



# The effect of geometric design and materials on section properties of additively manufactured lattice elements

Abduladheem Almalki<sup>1</sup> · David Downing<sup>1,2</sup> · Jordan Noronha<sup>1</sup> · Jason Dash<sup>1</sup> · Bill Lozanovski<sup>1,2</sup> · Rance Tino<sup>1,2,3</sup> · Ahmad Alghamdi<sup>4</sup> · Mahyar Khorasani<sup>1</sup> · Ma Qian<sup>1</sup> · Milan Brandt<sup>1,2</sup> · Martin Leary<sup>1,2</sup>

Received: 19 August 2022 / Accepted: 9 March 2023 / Published online: 3 April 2023  
© The Author(s) 2023

## Abstract

Additive manufacturing (AM) technologies such as laser-based powder bed fusion (LB-PBF) facilitate the fabrication of complex lattice structures. However, these structures consistently display dimensional variation between the idealised and as-manufactured specimens. This research proposes a method to characterise the impact of common LB-PBF powders (aluminium and titanium alloys) and geometric design parameters (polygon order, effective diameter, and inclination angle) on section properties relevant to stiffness and strength of as-manufactured strut elements. Micro-computed tomography ( $\mu$ CT) has been applied to algorithmically characterise the as-manufactured variation and identify a scale threshold below which additional geometric resolution does not influence the section properties of as-manufactured parts. This methodology provides a robust and algorithmic design for additive manufacturing (DFAM) tool to characterise the effects of manufacturing and design parameters on the functional response of AM strut elements, as is required for certification and optimisation.

**Keywords** Laser-based powder bed fusion · Additive manufacturing · Geometric analysis · Micro-computed tomography · Additive manufacturing defects · Design for additive manufacturing

## Nomenclature

AM	Additive manufacturing
BJT	Binder jetting technology
CAD	Computer-aided design
CSP	Cold spray
DED	Directed energy deposition
DFAM	Design for additive manufacturing
DOE	Design of experiments
IQR	Interquartile range
LB-PBF	Laser-based powder bed fusion
MAM	Metal additive manufacturing
MEX	Material extrusion
MJF	Multi jet fusion

MJT	Material jetting technology
PBF	Powder bed fusion
PBS	Powder bed system
PFS	Powder feed system
SEM	Scanning electron microscope
SHL	Sheet lamination
WFS	Wire feed system
$\mu$ CT	Micro-computed tomography

## Notation

Term	Definition	Unit
$A_{CT}$	Cross-sectional area of the as-manufactured case	$\text{mm}^2$
$A_{ideal}$	Cross-sectional area of the idealised case	$\text{mm}^2$
$C_p$	Specific heat	$\text{J}/(\text{kg}\cdot\text{K})$
$D_{eff}$	Effective diameter	$\text{mm}$
$h$	Thermal diffusivity	$\text{m}^2/\text{s}$
$I$	Second moment of area	$\text{mm}^4$
$I_{CT}$	Second moment of area of the as-manufactured case	$\text{mm}^4$
$I_{CT,max}$	Maximum second moment of area of the as-manufactured case	$\text{mm}^4$
$I_{CT,min}$	Minimum second moment of area of the as-manufactured case	$\text{mm}^4$

✉ Abduladheem Almalki  
s3795686@student.rmit.edu.au

Martin Leary  
martin.leary@rmit.edu.au

<sup>1</sup> RMIT Centre for Additive Manufacture, RMIT University, Melbourne, Australia

<sup>2</sup> ARC Training Centre in Additive Biomanufacturing, Kelvin Grove, Australia

<sup>3</sup> MD Anderson Cancer Center, Houston, TX, United States

<sup>4</sup> Umm Al Qura University, Makkah, Saudi Arabia

$I_{\text{ideal}}$	Second moment of area of the idealised case mm <sup>4</sup>
$k$	Thermal conductivity W/K
$h$	Elastic bending shape factor mm <sup>4</sup> /mm <sup>4</sup>
$\varnothing_B^e$	Elastic bending shape factor of the as-manufactured case mm <sup>4</sup> /mm <sup>4</sup>
$\varnothing_{B,\text{ideal}}^e$	Elastic bending shape factor of the idealised case mm <sup>4</sup> /mm <sup>4</sup>
$\varnothing_B^f$	Failure bending shape factor mm <sup>3</sup> /mm <sup>3</sup>
$\varnothing_{B,\text{CT}}^f$	Failure bending shape factor of the as-manufactured case mm <sup>3</sup> /mm <sup>3</sup>
$\varnothing_{B,\text{ideal}}^f$	Failure bending shape factor of the idealised case mm <sup>3</sup> /mm <sup>3</sup>
$p$	Polygon order integer
$R_g$	Radius of gyration mm
$R_{g,\text{CT}}$	Radius of gyration of the as-manufactured case mm
$R_{g,\text{ideal}}$	Radius of gyration of the idealised case mm
$s$	Polygon side length mm
$Z$	Section modulus of any polygon shape mm <sup>3</sup>
$Z_{\text{ideal}}$	Section modulus of the idealised case mm <sup>3</sup>
$Z_{\text{circle}}$	Section modulus of the circle of equal area mm <sup>3</sup>
$\alpha_{\text{ap}}$	Apparent angle degree
$\alpha_{\text{ed}}$	Edge angle degree
$\alpha_{\text{in}}$	Inclination angle degree
$\theta_{\text{rotation}}$	Rotation angle degree
$\rho$	Density kg/m <sup>3</sup>

## 1 Introduction

Additive manufacturing (AM) enables the layer-by-layer fabrication of three-dimensional geometry directly from computer-aided design (CAD) data, thereby providing potential advantages over conventional manufacturing [1]. For example, AM can fabricate complex, topology-optimised geometry as a single structure, whereas conventional manufacturing may be constrained by the need for tooling access [2]. Despite these advantages, AM processes are subject to a series of technical challenges including relatively low production rates, thermal stresses, potentially high material costs, and geometric uncertainties in the as-manufactured geometry [3]. Metal additive manufacturing (MAM) enables fabrication in a range of fusible metal alloys including light alloys, superalloys, and tool steels. As such, MAM is well suited for the fabrication of high-value lattice applications including medical implants, aerospace components, and custom tooling [4]. While understanding MAM defects within individual lattice strut elements is required to optimise mechanical performance, few fundamental studies have been executed, and the existing studies typically focus on

geometric properties rather than the fundamental section properties that determine structural performance.

In response to this shortcoming, a methodology is proposed to algorithmically quantify the section properties, including the second moment of area and shape factor of as-manufactured strut elements. This methodology is demonstrated with a design of experiments (DOE) that considers a range of design-relevant control factors for strut elements fabricated by laser-based powder bed fusion (LB-PBF), including various cross-section shapes (triangular face up, triangular face down, square, octagonal, and circle), materials (AlSi10Mg and Ti6Al4V), and strut element inclination angles,  $\alpha_{\text{in}}$  (35°, 45°, 90°). To enable the algorithmic characterisation of the geometric attributes of these as-manufactured lattice strut elements, micro-computed tomography ( $\mu$ CT) imaging techniques are applied to characterise the three-dimensional geometry of manufactured specimens [5]. This outcome contributes to the fundamental understanding of analytical and as-manufactured quantification methods for AM strut elements, as well as providing a robust DFAM tool for lattice certification and structure optimisation.

### 1.1 Metal additive manufacturing

As a sub-classification of AM, MAM processes sequentially fabricate three-dimensional metal components based on digital CAD data [6, 7]. Fabrication using MAM is typically achieved by the iterative fusion, or adhesion, of metallic input material over a series of layers based on cross-sections taken from digital design data [7]. Prominent examples include sheet lamination (SHL), binder jet technology (BJT), material jetting technology (MJT), material extrusion (MEX), powder bed fusion (PBF), and directed energy deposition (DED) [8]. MAM provides an opportunity to fabricate novel, mass-optimised, or high-value components such as medical implants and lightweight aerospace components. In this research, LB-PBF is used to fabricate individual strut element specimens due to the compatibility of this method with the fabrication of high-resolution features at small scales with a high degree of dimensional control [9].

As with any manufacturing process, defects occur during the MAM process due to complex physical phenomena and process parameters such as laser power, scan speed, hatch spacing, powder features, powder packing arrangements, density distribution, morphology, and thickness. This results in a high possibility of defect formation [10]. Echeta et al. [11] classified LB-PBF defects into three categories: porosity or incomplete fusion, residual stresses, and surface texture. Zhang et al. [10] defined this porosity as spheroidal voids within the fused powder, where the pore diameter is up to approximately 100  $\mu\text{m}$ . This porosity is formed due to high cooling rates during solidification, leading to dissolved

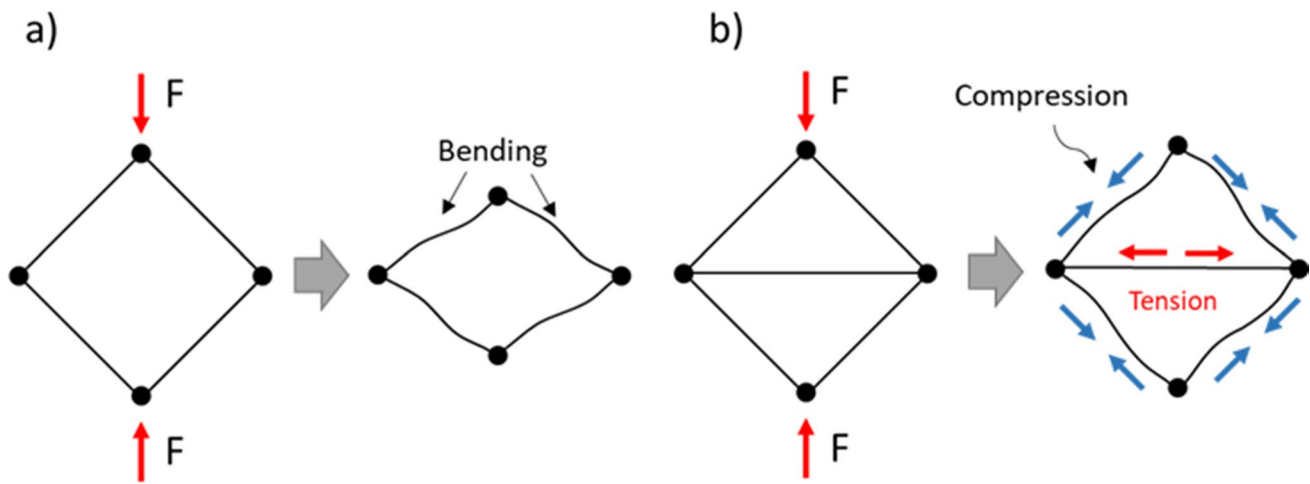


**Fig. 1** Bending-dominated (a) and stretch-dominated (b) mechanical response of lattice strut elements in response to an applied external load  $F$  [24]

gas that cannot escape from the melt pool which results in voids once the melt pool has solidified. Additionally, insufficient input energy may lead to incomplete fusion and can result in pores in the order of 500  $\mu\text{m}$ . Insufficient energy density or using inappropriate process parameters may cause balling effects on the surface of the fabricated object. The main driving mechanism for a balling defect in LB-PBF is Rayleigh instability and a lack of wetting which produces a segmented melt pool with the associated formation of ball shapes [12, 13]. Residual stresses are formed during the PBF processes due to rapid temperature cycling rates that can cause cracking in lattice strut elements [14, 15]. Furthermore, shrinkage occurs during the phase transition from a liquid melt pool to a solid structure, potentially leading to surface cracking. Surface texture variation is observed on MAM lattice structures, which is caused by several phenomena. Layer-wise fabrication methods employed during MAM inherently lead to the stair-stepping phenomenon [11, 16]. This is most clearly observed on surfaces inclined to the build direction, with a distinct characteristic surface roughness on both sides of the inclined surface of a lattice structure [17]. The magnitude of roughness on both the upward and downward faces of struts is a function of the inclination angle as well as the associated process parameters. This as-manufactured roughness may provide advantages in biomedical applications where it can be beneficial as a biomimetic surface encouraging cellular adhesion [18].

The primary commercial opportunity for AM production is typically high-value applications; consequently, methods to predict and quantify the magnitude and influence of AM defects in as-manufactured components are of critical importance [19, 20]. Echeta et al. [11] comprehensively reviewed the primary measurement methods available for quantifying MAM defects. These methods include  $\mu\text{CT}$ , scanning

electron microscope (SEM), physical inspection, optical microscopy, and Archimedes' method. Each of these methods has a specific set of capabilities for quantifying certain attributes of observed manufacturing defects. For this research,  $\mu\text{CT}$  provides a robust tool to quantify the geometric defects introduced during MAM and to characterise the associated section properties.

## 1.2 Mechanical response of lattice strut elements

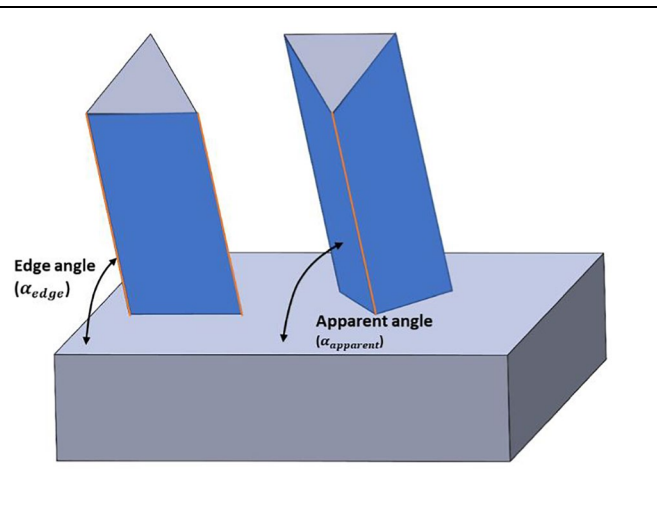
Lattice structures are commonly employed in applications subject to compressive or absorption loading conditions. The mechanical response of individual strut elements depends on the associated unit cell topology and loading conditions. The strut element loading response can be categorised as either bending-dominated or stretch-dominated [21], resulting in strut elements subjected predominantly to bending moments or axial loads, as illustrated in Fig. 1a,b, respectively. The structural response of the lattice can be predicted by Maxwell's stability criterion which considers pin-jointed structures and predicts the determinacy of the structure based on the number of struts and nodes [22, 23]. Strut element cross-section properties contribute substantially to structural response, especially for bending and buckling modes. This research provides insight into the structural efficiency of as-manufactured strut elements according to the associated material and geometric design parameters.

## 1.3 Strut cross-section manufacturability

Alghamdi et al. [5] investigated the effect of polygon order,  $p$  (triangular, square, octagonal, and circular), on the geometry of as-manufactured lattice strut elements fabricated with LB-PBF in aluminium alloy AlSi10Mg, and titanium

**Table 1** Effect of apparent angle (blue faces) and edge angle (orange edges) on the manufacturability of triangular sections with the vertex pointing upward and downward

Inclination angle ( $\alpha_{in}$ )	Edge angle ( $\alpha_{ed}$ )	Apparent angle ( $\alpha_{ap}$ )	Polygon shape
35°	35°	35°	▲
35°	35°	65.36°	▼
45°	45°	45°	▲
45°	45°	69.3°	▼
90°	90°	90°	▲
90°	90°	90°	▼



alloy Ti6Al4V. They observed the tendency for nominally triangular and square cross-sections to become circular upon fabrication, as quantified by the isoperimetric quotient.<sup>1</sup> This observed effect was particularly strong in the aluminium strut elements and for relatively small cross-sectional areas. Furthermore, triangular cross-sections were observed to have greater manufacturability when the triangle is oriented with a vertex pointing down (towards the build platen), compared to a vertex pointing up (away from the build platen). The enhanced manufacturability observed for vertex down triangular sections appears to be due to a combination of cross-sectional area and apparent inclination angle, where the vertex down triangles show an increase in the apparent inclination angle of the associated facets (Table 1). This reflects to the manufacturability of triangular strut elements vertex downward has fewer defects compared with vertex upward.

## 2 Geometric properties of polygon's cross-section

Section properties are the quantities that can be derived from the distribution of area in the cross-section of a given column or beam. They can be used to characterise structural design efficiency, including the second moment of area,  $I$ ; the radius of gyration,  $R_g$ ; section modulus,  $Z$ ; elastic shape

factor,  $\phi_B^e$ ; and failure shape factor,  $\phi_B^f$ . These properties will be calculated to analytically compare the efficiency of the specimens assessed in this research and are briefly defined below.

### 2.1 Second moment of area

The second moment of area is a measure of the capacity of a column to resist buckling and a beam to resist bending [25]. The planar second moment of area for a cross-section is defined as the integral sum of the squared distance,  $y$ , of infinitesimal area,  $dA$ , from the neutral axis (Eq. 1) [26]. For regular polygonal shapes, such as a circle of arbitrary radius,  $r$  (Eq. 2), the second moment of area can be calculated analytically. A general equation (Eq. 3) is introduced to obtain the second moment of area for any  $n$ -sided polygon<sup>2</sup> [27], where  $x_i$  and  $y_i$  represent the Cartesian coordinates of the  $i$ -th polygon vertex.

$$I = \int y^2 dA \quad (1)$$

$$I_{\text{circle}} = \frac{\pi}{4} r^4 \quad (2)$$

$$I_{\text{polygon}} = \frac{1}{12} \sum_{i=1}^n (x_i y_{i+1} - x_{i+1} y_i) (x_i^2 + x_i x_{i+1} + x_{i+1}^2) \quad (3)$$

<sup>1</sup> The isoperimetric quotient of a closed contour is the ratio of the contour area to the area of a circle of equal perimeter to the closed curve. It is a measure of 'circularity', where a circle yields an isoperimetric quotient of unity [25]. 25.Jywe, W.-Y., C.-H. Liu, and C.o.-K. Chen, *The min-max problem for evaluating the form error of a circle*. Measurement, 1999. 26(4): p. 273–282.

<sup>2</sup> The polygon points should be ordered in a counter-clockwise direction; voids are included by clockwise ordering.

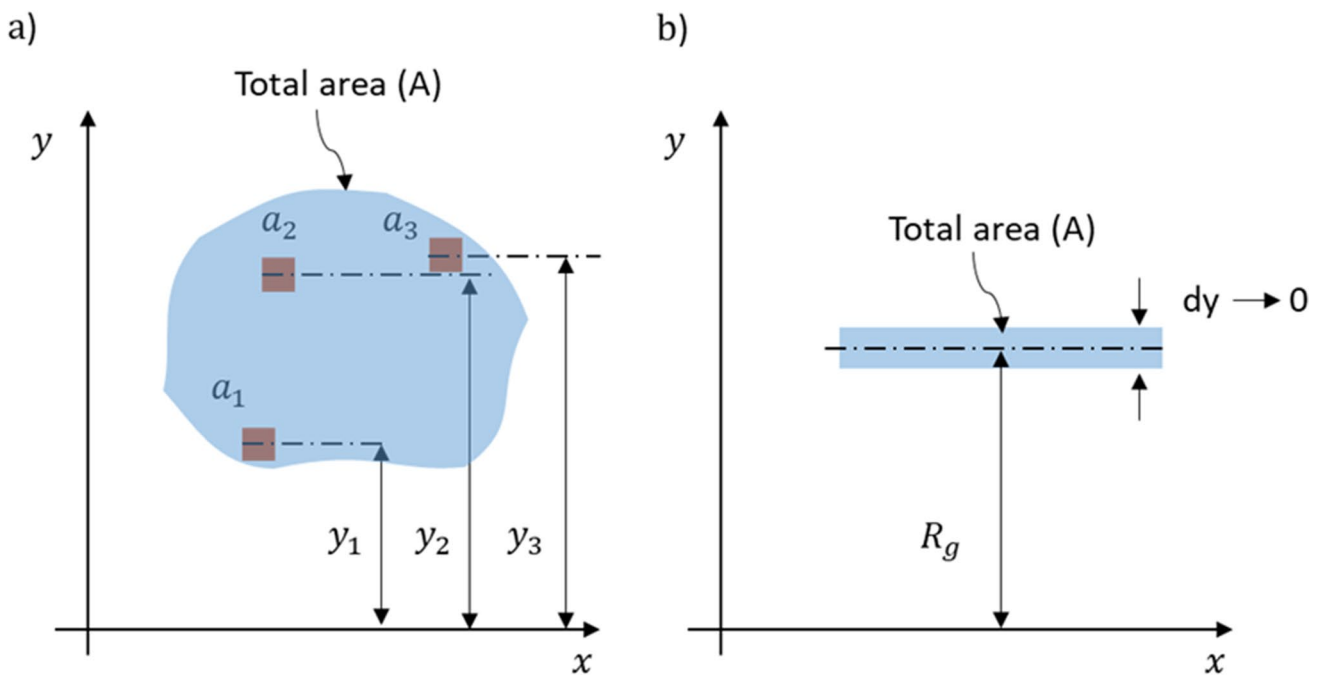


**Fig. 2** Radius of gyration schematic comparing (a) distances,  $y_i$ , from the  $x$ -axis for infinitesimal areas,  $a_i$ , taken from the cross-section and (b) equivalent area in an infinitesimal strip offset by the radius of gyration from the  $x$ -axis [ $dy \rightarrow 0$ ]

### 2.2 Radius of gyration

The radius of gyration defines the theoretical distance from the cross-section centroid at which the cross-sectional area can be considered to be concentrated to achieve an equal second moment of area as the actual cross-section distribution (Fig. 2b) [26]. It is a measure of the resistance of the cross-section to elastic buckling or bending [28, 29] and can therefore be useful to compare the resistance to buckling or bending of various sections with an equal cross-sectional area (Eq. 4).

$$R_g = \sqrt{\frac{I}{A}} \tag{4}$$

For example, comparing  $R_g$  for a triangular cross-section with that of a circular cross-section shows that triangular sections have larger  $R_g$ , indicating they are more efficient when resisting elastic buckling or bending than a circular section with equal area.

### 2.3 Elastic and failure shape factors for bending

The shape factors compare the mechanical performance (such as stiffness and failure under buckling or bending) of a cross-section of interest against a reference circular cross-section of the equivalent area [30]. The shape factors

of a solid circular cross-section are unity and changes with cross-section shape. When the shape factor increases, the resistance to bending and buckling increases. In addition, the dimensionless nature of shape factors allows for the comparison of shapes independent of scale. The influence of cross-section shape on stiffness can be calculated using the elastic bending shape factor,  $\phi_B^e$  (Eq. 5). As strength depends on local stress, the section modulus,  $Z$ , must be calculated (Eq. 6), where  $y_{max}$  is the outermost fibre from the neutral axis subject to compression or tension to quantify the bending failure shape factor,  $\phi_B^f$ . This is the ratio of any given section modulus over that of a circle of equal area (Eq. 7),  $Z_{circle}$ .

$$\phi_B^e = \frac{4\pi I}{A^2} \tag{5}$$

$$Z = \frac{I}{y_{max}} \tag{6}$$

$$\phi_B^f = \frac{4\sqrt{\pi}Z}{A^{3/2}} = \frac{Z}{Z_{circle}} \tag{7}$$

Structural performance in bending can therefore be characterised by selecting an appropriate combination of material and shape for both elastic and failure scenarios [30]. In the “3.3” section, it is shown that the solid triangular cross-section under bending load is stiffer than an equivalent solid

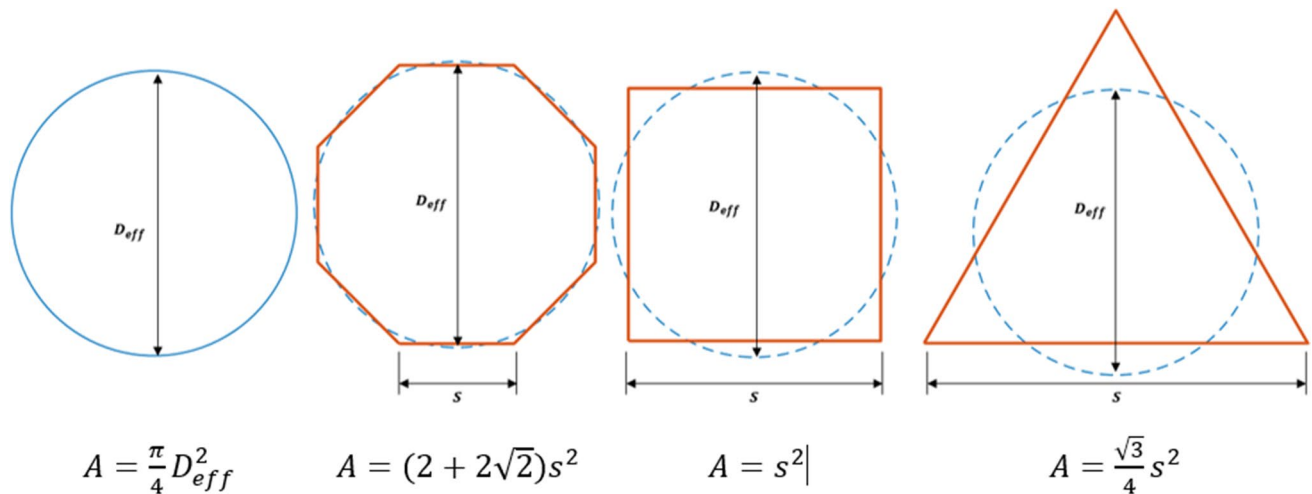


**Fig. 3** Circles of effective diameter,  $D_{eff}$ , superimposed onto polygons of equivalent area

circular cross-section by 21%, whereas it has 23% lower strength.

## 2.4 Effective diameter

Effective diameter,  $D_{eff}$ , represents the diameter of a circle that has an equivalent area to that of the cross-section of interest. In this research, four effective diameters are implemented (3.0 mm, 2.0 mm, 1.0 mm, and 0.5 mm) for four different cross-sections (circular, octagonal, square, and triangular) with equivalent areas [5] (Fig. 3).

$$A = \frac{\pi}{4} D_{eff}^2 \quad A = (2 + 2\sqrt{2})s^2 \quad A = s^2 \quad A = \frac{\sqrt{3}}{4} s^2$$

## 3 Method

Recent literature reviews have highlighted a lack of DFAM tools that can quantify the structural integrity of as-manufactured AM strut elements. Cross-section design has a significant impact on strut performance; thus, the shape factor of as-manufactured strut elements should be characterised to assess the strength and stiffness of proposed designs. This research proposes a fundamental methodology for the characterisation of as-manufactured strut elements to quantify the associated geometric and functional properties. This generalisable DFAM tool is implemented specifically on strut element specimens fabricated by PB-LBF. Figure 4 illustrates the proposed methodology's workflow, which can be applied as a guideline to any manufacturing process to ensure optimal production and certification. The

proposed method can be classified into the following steps: CAD design, analytical quantification, PB-LBF fabrication,  $\mu$ CT imaging, as-manufactured quantification, and statistical analysis.

## 3.1 Design of experiments

The methodology was implemented on a set of strut geometries designed, fabricated, and scanned in previous work [5]. The design of experiments (DOE) contains four control factors including two material types implemented separately as powder feedstock for the LB-PBF process (aluminium alloy AlSi10Mg and titanium alloy Ti6Al4V), three inclination angles ( $\alpha_{in} = 90^\circ, 45^\circ, 35^\circ$ ), four nominal diameters ( $D = 3.0, 2.0, 1.0, 0.5$  mm), and five polygonal cross-sections (circle, octagon, square, triangle vertex up, triangle vertex down). These specimens were arranged in rows dependent upon the inclination angle on a plate feature 3-mm thick and extruded from the plate by a length of 15 mm (Fig. 5), resulting in a total of 120 strut elements.

## 3.2 Laser-based powder bed fusion

An SLM Solutions 250HL machine was implemented to fabricate the Ti6Al4V struts, and an SLM Solutions 125HL machine manufactured the AlSi10Mg struts. The operational parameters for each machine are displayed in Table 2. Following fabrication, the parts were cooled within the machine to room temperature, and then electrical discharge machining (EDM) was utilised to wire cut the strut specimens from the build plate.



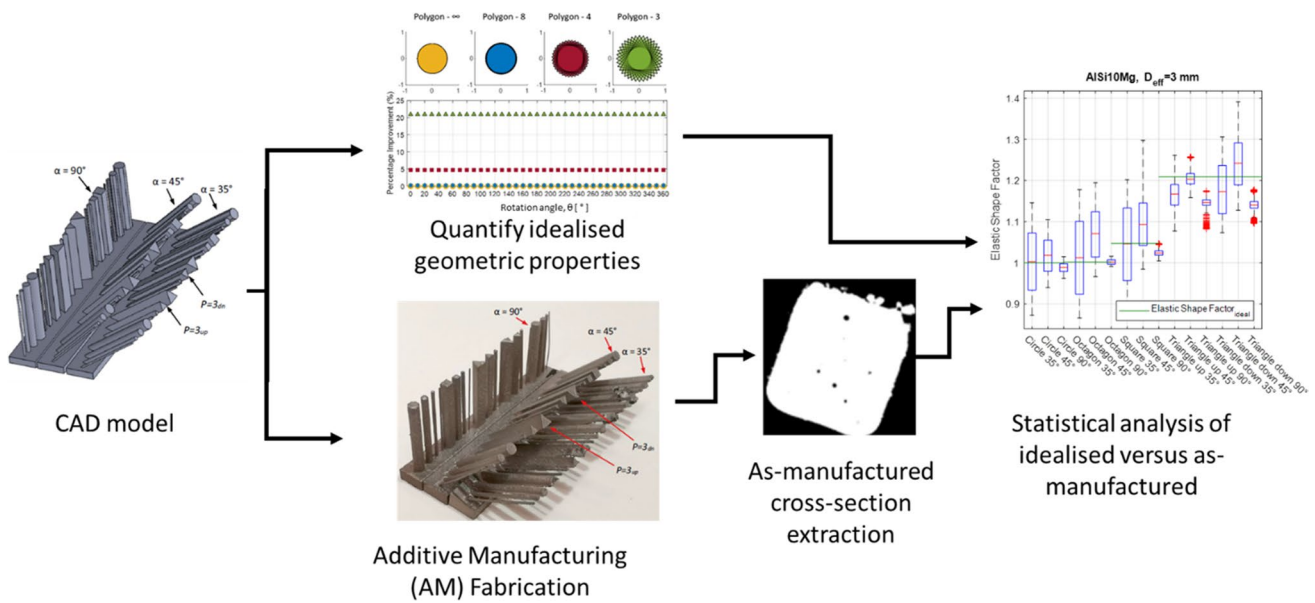


Fig. 4 Flow chart for the proposed method of quantifying cross-section properties for idealised and as-manufactured strut elements [5]

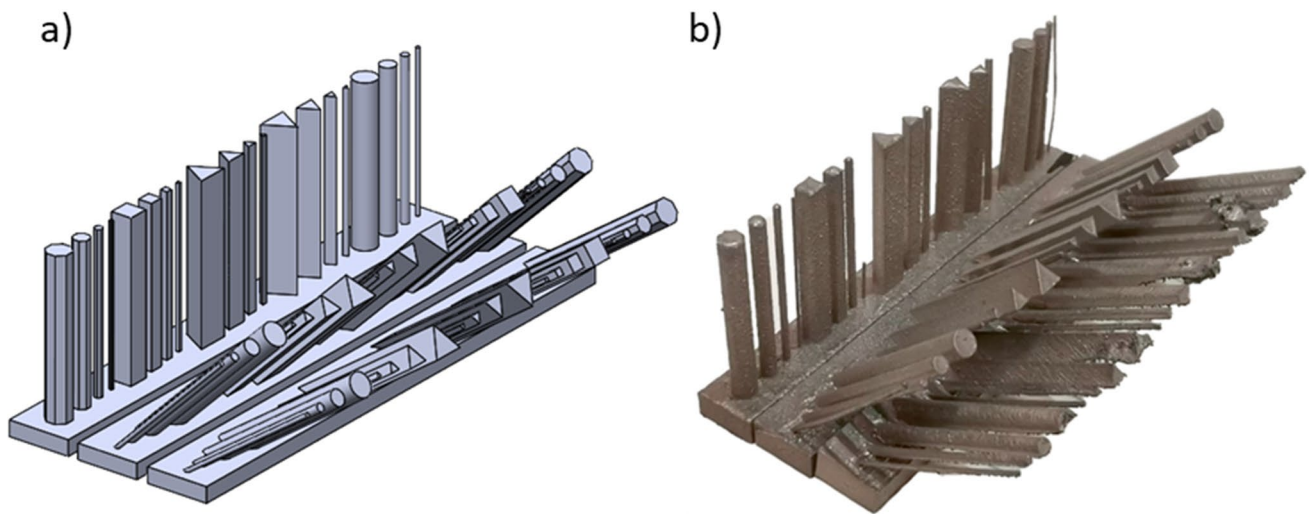


Fig. 5 CAD (a) and as-manufactured parts (b) of strut elements [5]

### 3.3 Laser scan strategy

A standard hatch infill scan strategy was implemented to fabricate these struts, as displayed in Fig. 6. Initially, a scan path is applied that follows the slice perimeter of the STL file (this scan is referred to as a border scan). To achieve a high geometrical accuracy to the idealised model, the border scan is inset from the nominal slice contour by 60 μm (Ti6Al4V) and 120 μm (AlSi10Mg) for melt pool compensation. An offset scan is then implemented, inset from the initial border scan by a further 90 μm (Ti6Al4V) and 150 μm (AlSi10Mg). A hatch pattern inclined at 90° is then

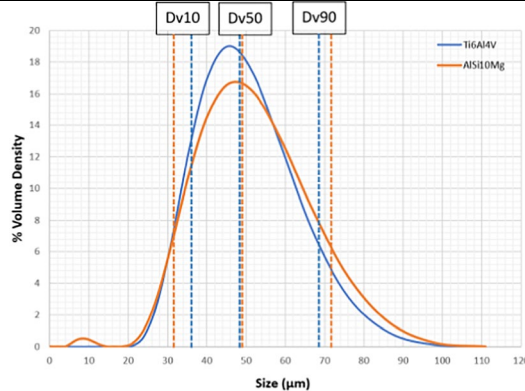
implemented to scan the remainder of the strut’s cross-sectional area. This hatch pattern is inset by 90 μm (Ti6Al4V) and 150 μm (AlSi10Mg) from the offset scan. To ensure complete melting, the hatching is rotated by 66.9° at each consecutive scan layer. Finally, a single contour scan tracing the hatch pattern perimeter is implemented to smooth the non-uniform edges of the hatch pattern.

### 3.4 Micro-computed tomography

To quantify the strut geometries, a Bruker SKYSCAN X-ray micro μCT machine (Bruker Pty Ltd.) was utilised.

**Table 2** LB-PBF parameters and associated powder size profile for both AISi10Mg and Ti6Al4V

Material	Ti6Al4V	AISi10Mg
Machine	SLM250	SLM125
Thermal conductivity, k (W/K)	7.2	140
Density, ρ (kg/m <sup>3</sup> )	4471	2680
Specific heat, Cp (J/kgK)	562	900
Thermal diffusivity, h (10 <sup>-6</sup> m <sup>2</sup> /s)	2.9	58
Layer thickness (μm)	30	50
Focal offset (μm)	0	2
Laser power (W)	175	350
Energy density (J/mm <sup>3</sup> )	68.5	40



**Ti6Al4V:** Dv10 = 48.9, Dv50 = 73.3, Dv90 = 110 (μm)  
**AISi10Mg:** Dv10 = 32.7, Dv50 = 49.5, Dv90 = 71.9 (μm)

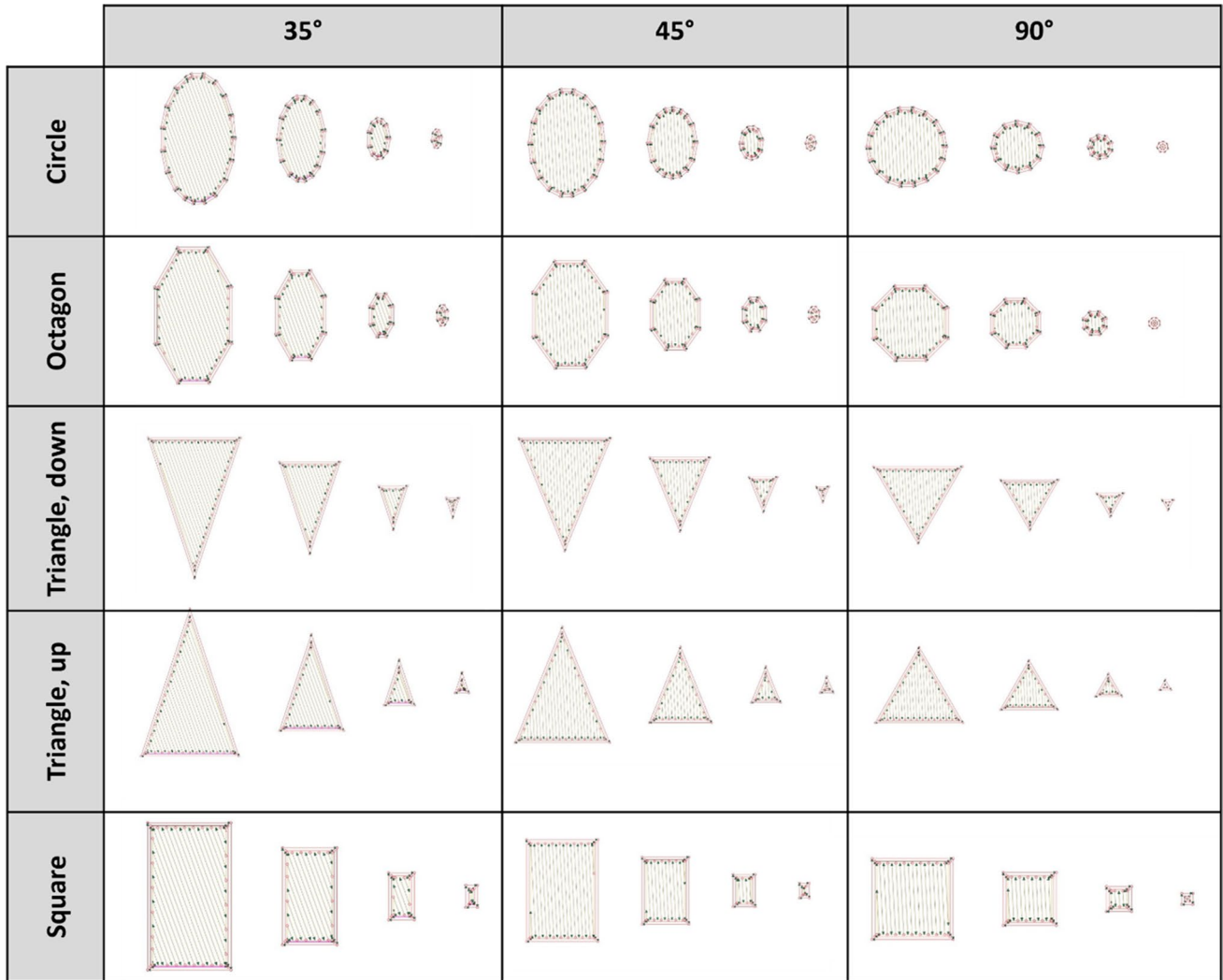


**Fig. 6** Laser scan strategy for the titanium and aluminium struts over a range of inclines (35°, 45°, 90°) for the effective diameters of 3 mm, 2 mm, 1 mm, and 0.5 mm (right to left), where the red lines are bor-

der scans, and green lines are the hatch pattern. In these images, the contour scan is coincidental with the hatch pattern and is not visible due to the overlap



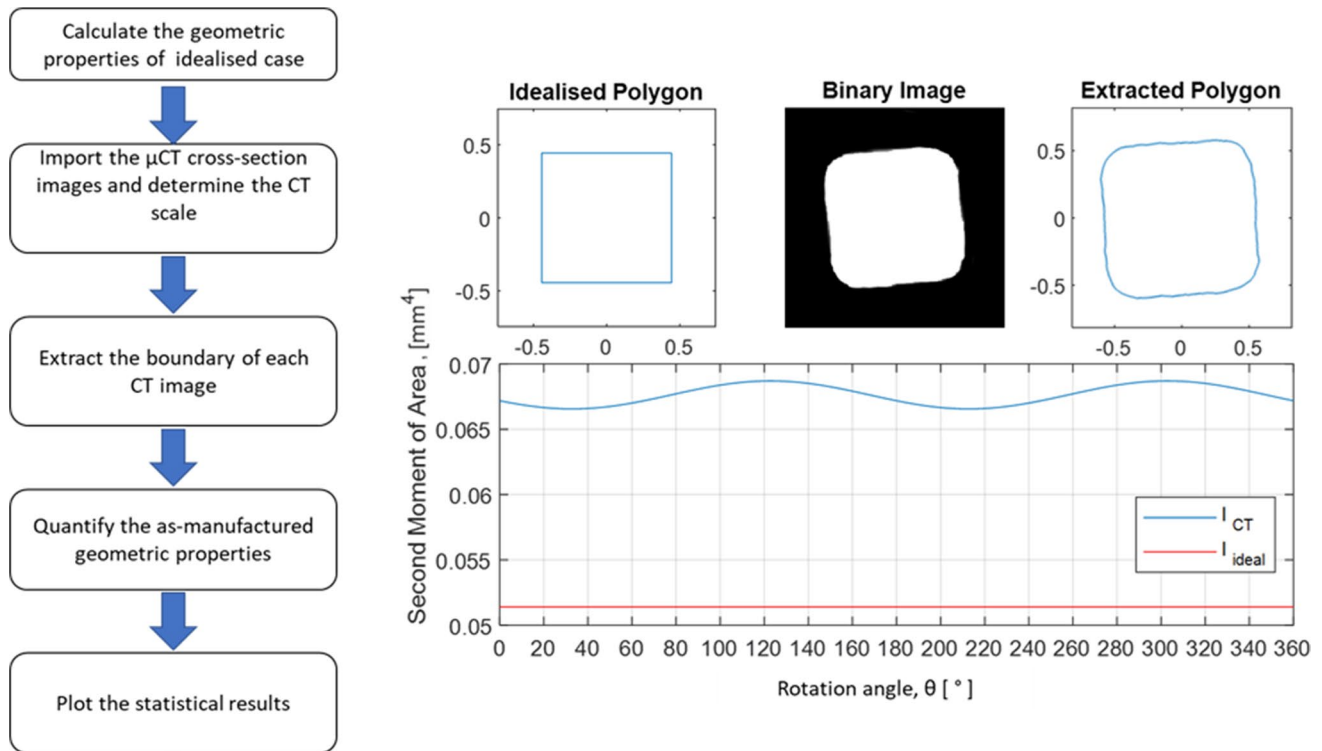


**Fig. 7** Algorithmic process for quantifying geometric properties of both idealised and as-manufactured cases

The technology used an X-ray tube current of 100  $\mu\text{A}$ , an acceleration voltage of 100 kV, and a pixel size of 8  $\mu\text{m}$ . The AlSi10Mg samples employed an Al 1-mm filter, while the Ti6Al4V samples used a Cu 1-mm filter. To reconstruct the cross-section slices acquired from the  $\mu\text{CT}$ , nRECON shadow image reconstruction software (Bruker Pty Ltd.) was used. Reconstructed grey scale images were then used to identify the strut element boundary and quantify the as-manufactured section properties.

### 3.5 Algorithmic implementation

The cross-section geometric properties for both idealised and as-manufactured cases are calculated using a MATLAB (R2020b) script [31] that was updated and customised for quantifying the section properties. The code starts by obtaining the idealised properties based on the polygon order from the DOE. Then,  $\mu\text{CT}$  cross-section images for the as-manufactured case are imported and converted into binary images. From this data, the geometric properties are calculated as a function of the angular orientation of the cross-section about its centroidal axis for the second moment of area (Fig. 7). To provide statistical distributions of cross-section response, this method is repeated sequentially on images within the image stack.

## 4 Observation and results

Section properties of the proposed DOE for both idealised and as-manufactured cases are presented in this section. It is divided into seven subsections: The idealised case, which demonstrates how polygon order affects the geometric properties; the comparison between idealised polygon cross-sections and as-manufactured strut element cross-sections for both materials; the second moment of area; the radius of gyration; the elastic shape factor, used to evaluate the stiffness of the as-manufactured geometry; the failure bending shape factor, used to evaluate the strength of the as-manufactured geometry; and main effect plots of section properties.

### 4.1 Geometric properties of idealised strut elements

The stiffness and strength of strut element specimens associated with the same cross-sectional area may be characterised by quantifying the idealised geometric properties including the second moment of area,  $I_{\text{ideal}}$ , the radius of gyration,  $R_{g,\text{ideal}}$ , elastic bending shape factor,  $\phi_{B,\text{ideal}}^e$ , section modulus,  $Z_{\text{ideal}}$ , and bending failure shape factor,  $\phi_{B,\text{ideal}}^f$ .

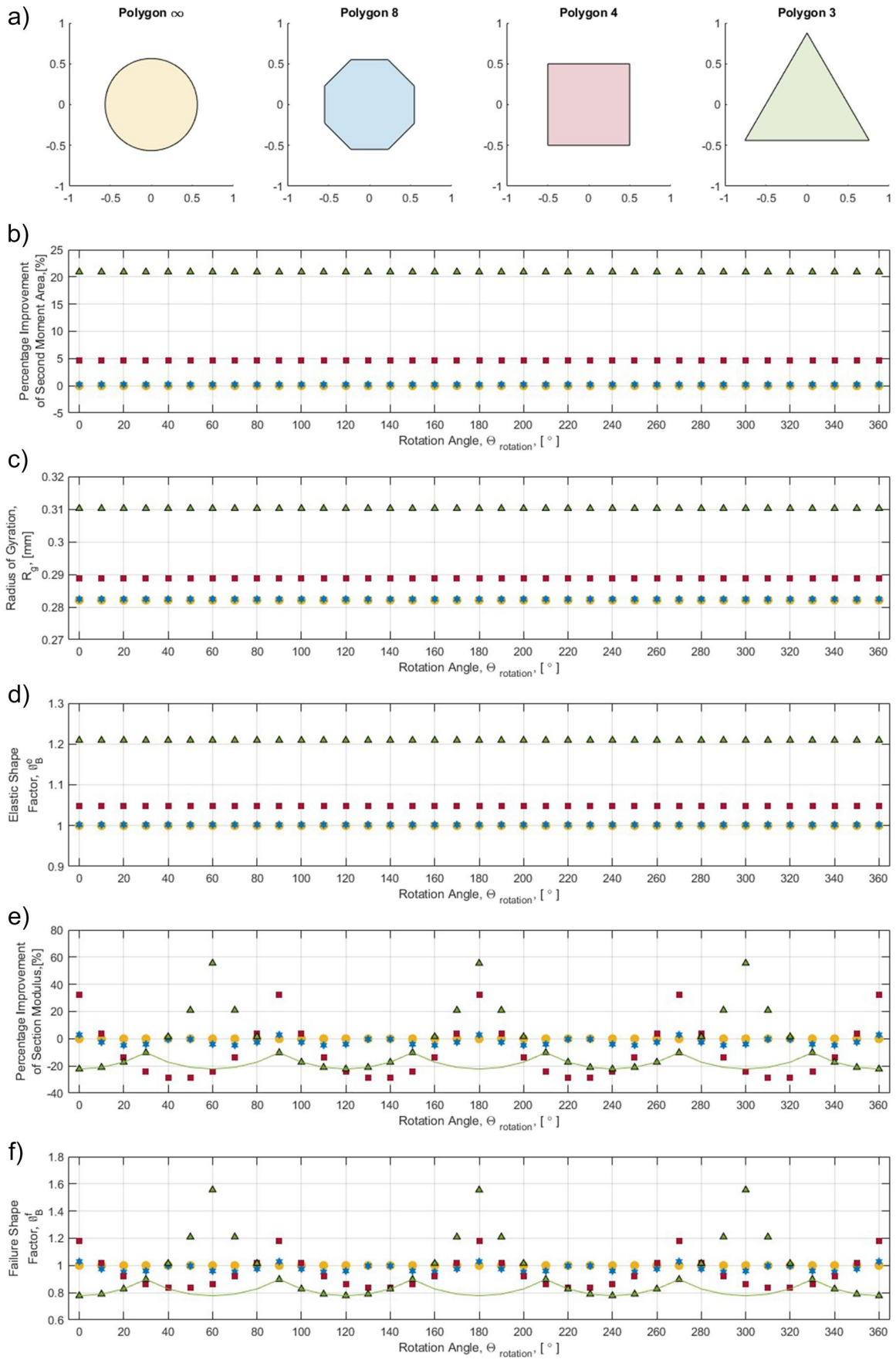


**Fig. 8** Idealised geometric properties for polygon orders rotated by  $\theta_{\text{rotation}}$ , where (a) circle, octagon, square, and triangle, associated with the same cross-sectional area, (b) second moment of area percentage improvement, over the circle, for each shape, (c) radius of gyration, (d) elastic shape factor, (e) percentage improvement of section modulus, over the circle, and (f) failure shape factor

These geometric properties are quantified in Fig. 8 for various regular polygonal cross-sections associated with the equal cross-sectional area, for a range of orientations achieved by incremental rotations,  $\theta_{\text{rotation}}$ , about the centroid. Figure 8b–d shows that the second moment of area, radius of gyration, and elastic shape factor all remain constant while rotating these idealised polygonal shapes. The elastic shape factor of the octagonal cross-section has a very slight increase of 0.2% over the circular section, whereas square and triangular shapes indicate 4.7% and 20.9% increases, respectively. The section modulus and failure shape factor show a dependency on the polygon's orientation that increases with lower-order polygons which is associated with vertex orientation. For example, the failure shape factor of the idealised triangular cross-section ranged from –23% lower (pointing up,  $\theta_{\text{rotation}} = 0^\circ, 120^\circ, 240^\circ$ ) to 55% higher (pointing down,  $\theta_{\text{rotation}} = 60^\circ, 180^\circ, 300^\circ$ ), when compared to that of the circular cross-section. These results evaluate the section modulus and shape factor based on the extreme fibres on one side of the neutral axis only. When the extreme fibres are considered from both sides simultaneously, the failure shape factor for the triangle, although orientation dependent, is always less than the circle, as indicated by the solid line in Fig. 8f. Although the triangular cross-section is 20.9% stiffer than the circle, it tends to fail in the weakest direction at 23% lower load compared with the circular cross-section (Fig. 8f). The concept of shape factors is well known in civil engineering but has yet been applied in the design of lattice structure elements fabricated by AM. The following subsections investigate how the as-manufactured cross-section varies from the idealised results for these important section properties.

## 4.2 Idealised versus as-manufactured cross-sectional area

The as-manufactured polygon cross-sectional area,  $A_{\text{CT}}$ , is affected by manufacturing processes, leading to variation between the idealised and as-manufactured strut elements. The effective diameter,  $D_{\text{eff}}$ , inclination angle,  $\alpha_{\text{in}}$ , polygon order,  $p$ , and material choice all significantly affect LB-PBF manufacturability.

Figure 9 shows the variation in the cross-sectional area within each of the as-manufactured strut elements. The box plots provide a graphical statistical summary for each cross-section image for the given strut. These include the

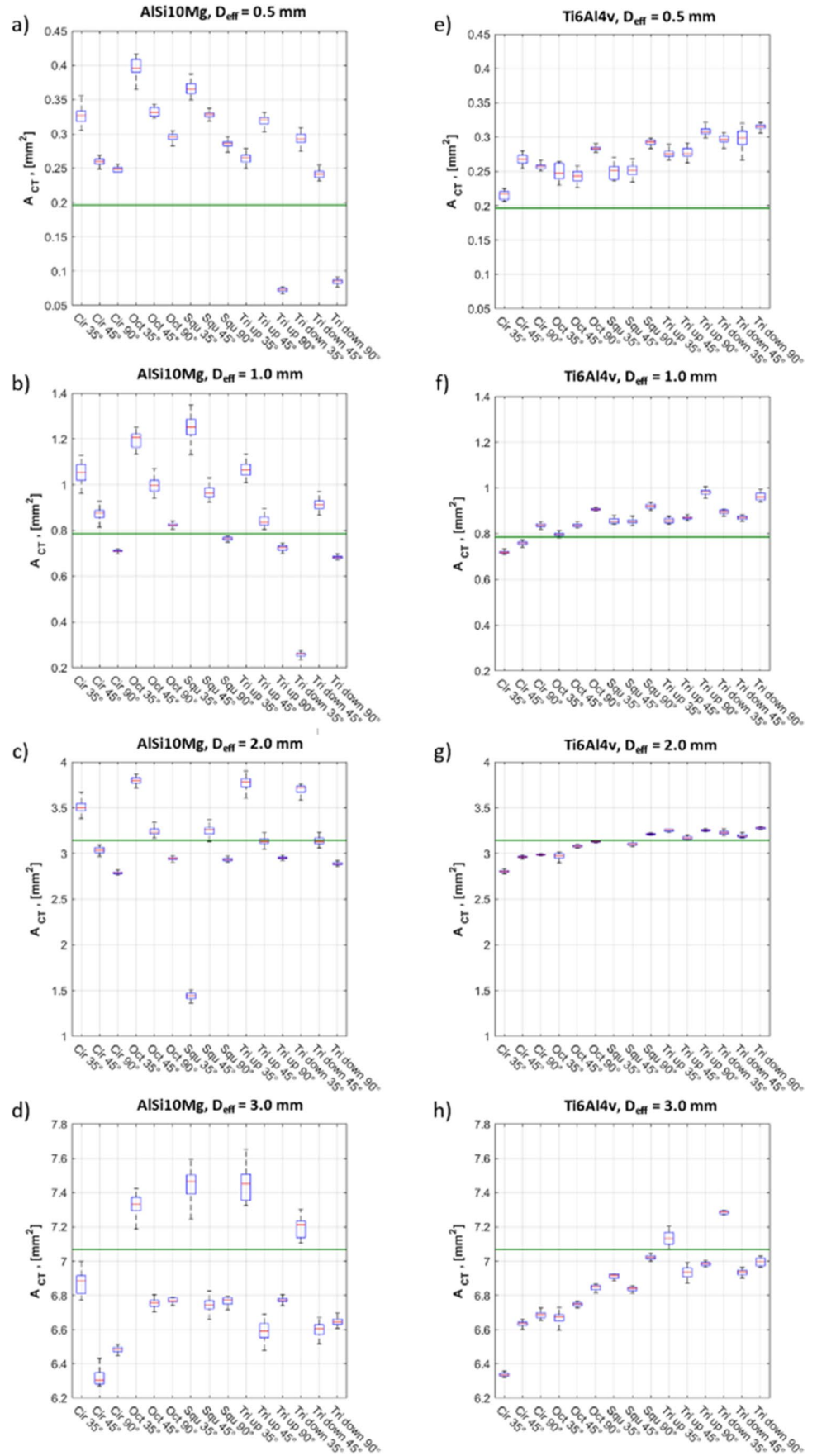
rectangular box representing the interquartile range (IQR) (25–75% percentiles), with the whiskers extending up to  $1.5 \times \text{IQR}$  and the median as the horizontal line within the box. The plots are presented in a graphical array as defined by material (columns) and effective diameter (rows), while cross-section shape and build inclination angle form the horizontal axis labels and the as-manufactured cross-sectional area forms the vertical axis labels. The expected value based on the idealised shape is presented as horizontal lines spanning the plots. For consistency, each of the sectional characteristics discussed in later subsections is presented using the same graphical array, with only the vertical axis changing to reflect the relevant value.

When comparing the aluminium (left column of Fig. 9a–d) to the titanium (right column of Fig. 9e–h) specimens, generally, there is greater variation within the individual aluminium specimens than in the titanium specimens, as indicated by the relative size of the IQR, the exception being at  $D_{\text{eff}} = 0.5\text{mm}$ . Furthermore, for the aluminium, there is a trend that area (median) and variation in the area (box plot size) increases with decreasing inclination angle. For the titanium (Fig. 9e–h), there is an upward trend in the position of the box plots within each graph, indicating that the cross-sectional area of the strut elements increases as the shape changes from circular to triangular, i.e., as the polygon order decreases, the area increases. This suggests that more material may be accumulating on the as-manufactured triangular shape than on the circular shape, even though they are intended to be the same area as indicated by the spanning horizontal line. For the aluminium strut elements (Fig. 9a–d), the same upward trend across the shapes is not visible; however, within each shape (clusters of three), there is both a downward trend in the cross-sectional area and in the variation of the cross-sectional area with increasing build inclination angle. These trends indicate that the cross-sectional area of aluminium strut elements is strongly affected by inclination, accumulating more area and greater variation in the area along a strut element as the build inclination angle is decreased from  $90^\circ$  to  $35^\circ$ . Meanwhile, the titanium strut elements show far less variation in the area.

## 4.3 Second moment of area (ideal versus CT)

The second moment of area for as-manufactured case,  $I_{\text{CT}}$ , is calculated based on extracted data from  $\mu\text{CT}$  cross-section images. This extracted data provides the outer boundary, centroid, and as-manufactured area,  $A_{\text{CT}}$ , for each image. Each fabricated strut element is imaged many times along its length. Therefore, to quantify  $I_{\text{CT}}$  with image orientation, the extracted boundary is incrementally rotated by a small rotation angle,  $\theta_{\text{rotation}}$ , ( $3.6^\circ$ ), as shown in Fig. 10a. At each rotational angle, the  $I_{\text{CT}}$  is calculated, as shown in Fig. 10b.

**Fig. 9** Box plots of  $A_{CT}$  compared with  $A_{ideal}$  (green horizontal lines), where (a) to (d) are aluminium strut elements, with an effective diameter of 0.5 mm, 1.0 mm, 2.0 mm, and 3.0 mm, and (e) to (h) are titanium strut elements, with an effective diameter of 0.5 mm, 1.0 mm, 2.0 mm, and 3.0 mm (outliers hidden)



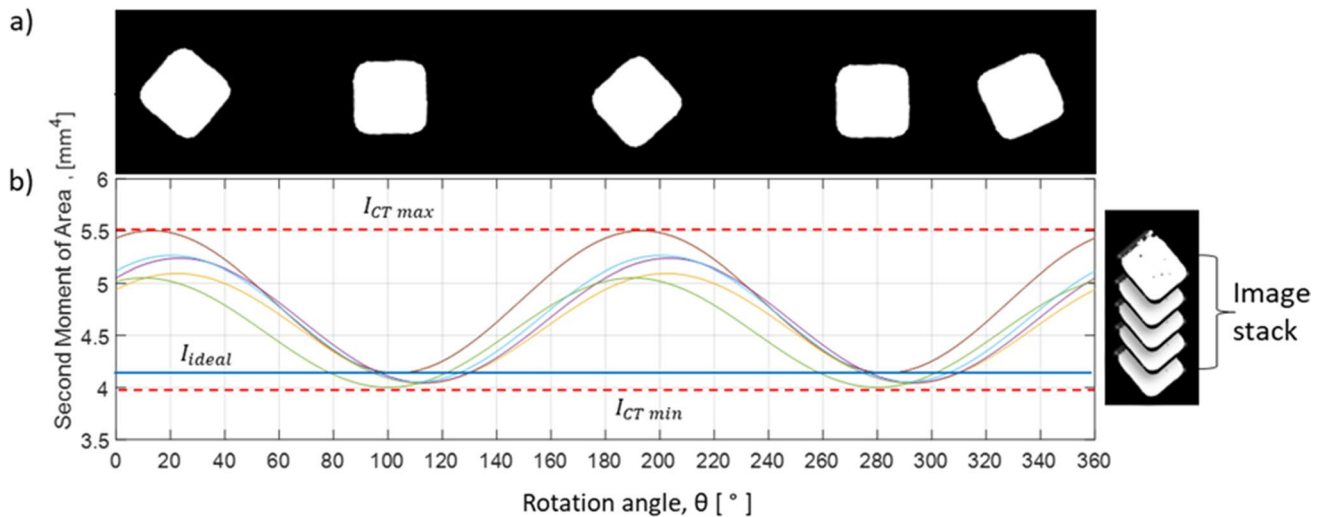


**Fig. 10** Second moment of area of as-manufactured strut element where maximum  $I_{CT,max}$  and minimum  $I_{CT,min}$  are denoted with red dash lines; idealised  $I_{ideal}$  represented with a solid blue line; the coloured lines represent  $I$  for each image in the stack at rotation  $\theta_{rotation}$ ;

**(a)** cross-section image showing key rotations in the graph; **(b)** second moment of area plotted over all possible rotations for as-manufactured and idealised cases

All values of  $I_{CT}$  are compared with those of the idealised case of a circular cross-section,  $I_{ideal}$ , for each strut, categorised by material (AlSi10Mg and Ti6Al4V),  $D_{eff}$ , shape,  $\alpha_{in}$ , as shown in Fig. 11. The distribution of  $I_{CT}$  is presented in the form of box plots, using the same graphical array described in the “Idealised versus as-manufactured cross-sectional area” section.  $I_{ideal}$  is shown as horizontal line segments that increase with decreasing polygon order.

Comparing the aluminium and titanium struts at the same effective diameter, there is significantly more variation in  $I_{CT}$  across the aluminium struts than across the titanium struts, suggesting that titanium provides a more consistent stiffness. The aluminium strut elements seen in Fig. 11a–d show both  $I_{CT}$  and  $A_{CT}$  experience a similar trend. The magnitude and variation of  $I_{CT}$  within the as-manufactured strut elements show a decreasing trend with increasing build inclination. This is seen by longer IQR boxes for 35° strut elements compared to the 90° struts. Considering the titanium strut elements in Fig. 11e–h, the increase in  $I_{CT}$  across the shapes is greater than expected, in comparison to the idealised cross-section. This corresponds with the previous observation that the as-manufactured area,  $A_{CT}$ , increased with decreasing polygon order at a given  $D_{eff}$ .

#### 4.4 Radius of gyration (ideal versus CT)

The efficiency of a cross-section shape of interest for elastic stability under compression can be evaluated using the radius of gyration,  $R_g$ , associated with the cross-sectional area of interest, as discussed in the “Introduction” section.

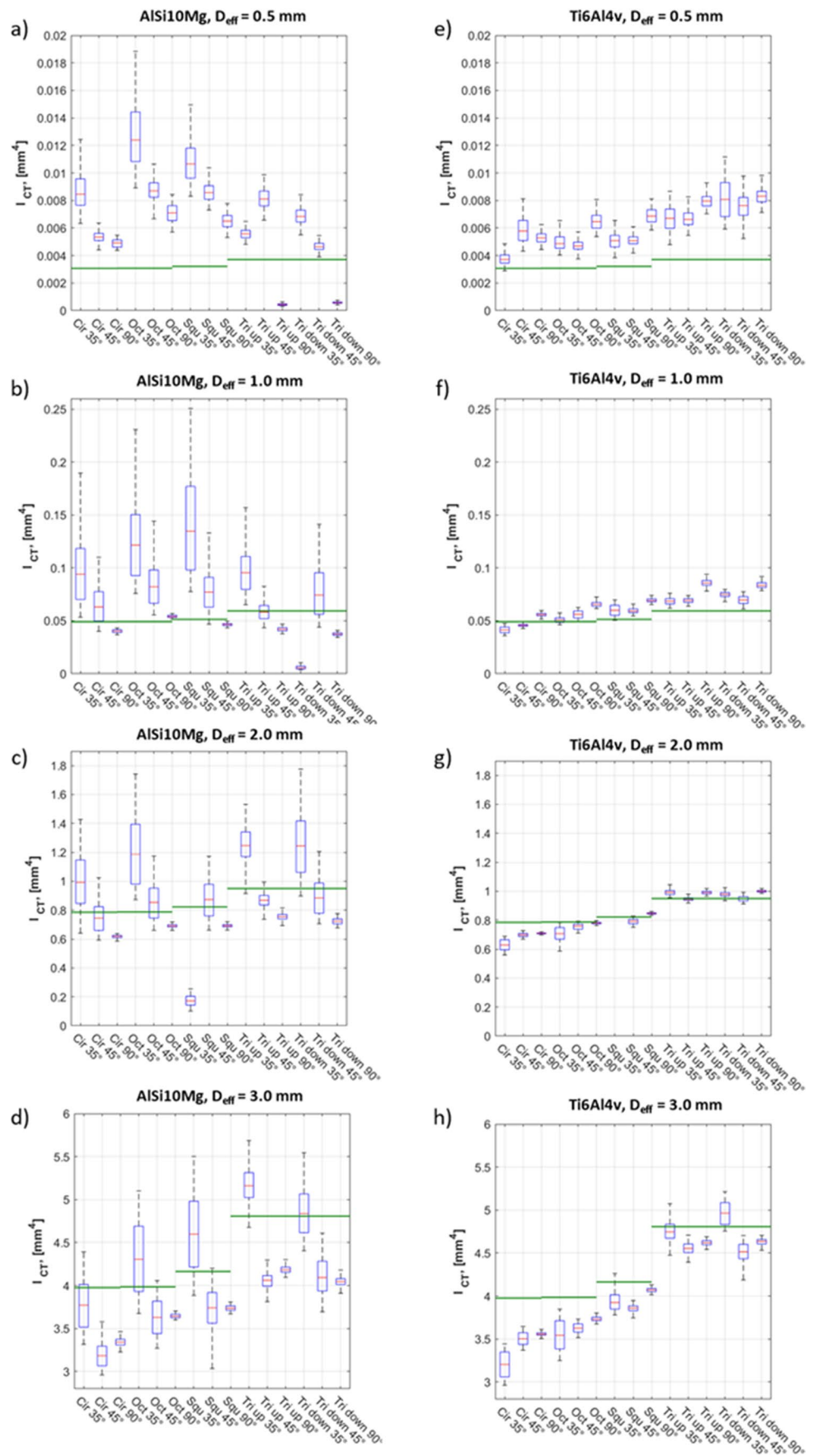
Figure 12 shows box plots for the radius of gyration of the as-manufactured strut elements,  $R_{g,CT}$ , compared with the idealised case,  $R_{g,ideal}$ , represented as a green horizontal line segment for both aluminium and titanium. It is useful to evaluate the efficiency of the actual shape versus the idealised shape as it does not consider the material. Figure 12 also evaluates the quality of fabrication and the effectiveness of controlling factors such as  $\alpha_{inc}$ . Overall, it can be observed that the variation in  $R_{g,CT}$  is larger in the aluminium (Fig. 12a–d) than the titanium (Fig. 12a–d) strut elements. The variation within individual aluminium strut elements is largest for the 35° and 45° build inclination angle, while the 90° cases are similar to the titanium.

#### 4.5 Elastic shape factor (ideal versus CT)

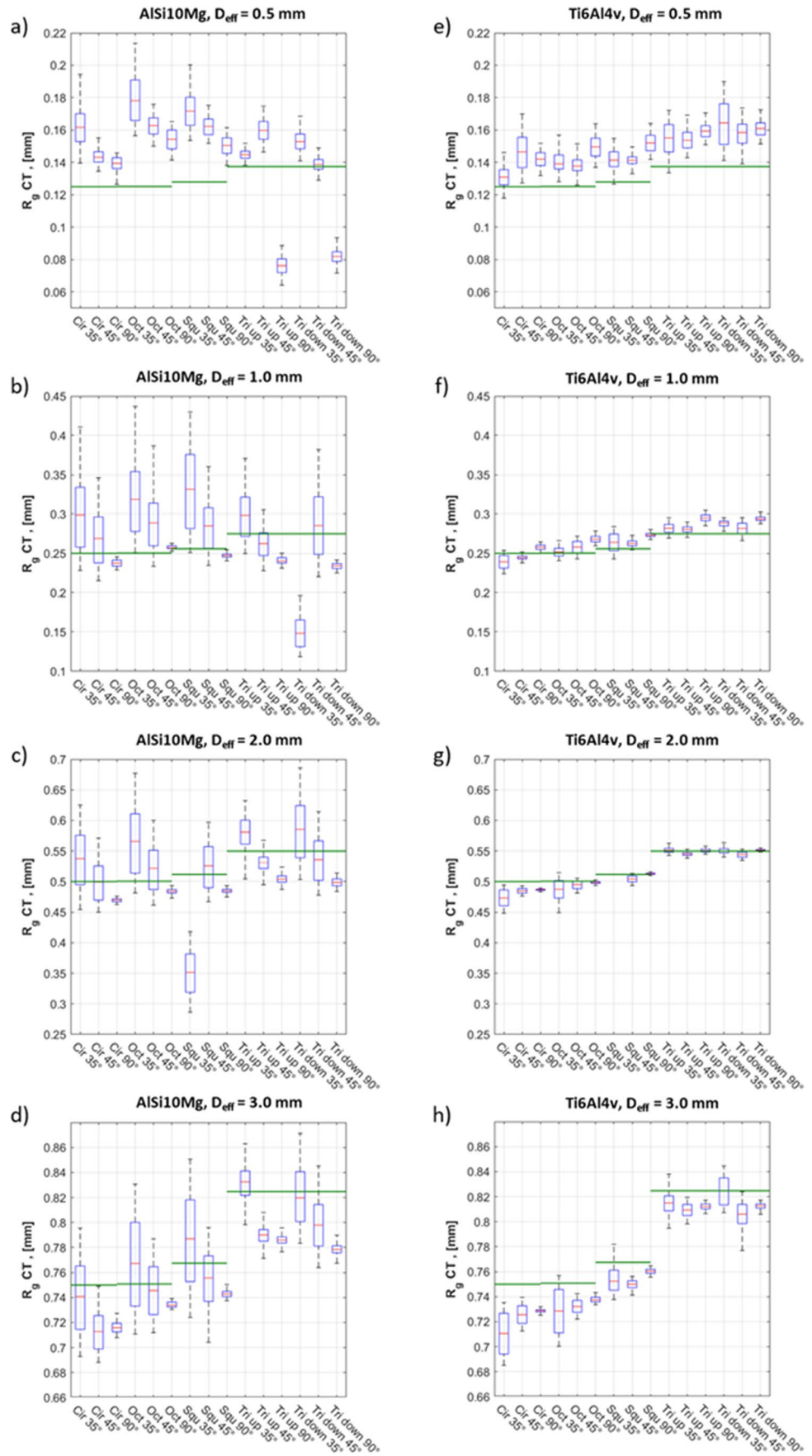
The elastic shape factor,  $\varnothing_B^e$ , provides a measure of the stiffness efficiency of the cross-section shape, as discussed previously in the “2.1” section. The as-manufactured elastic shape factor,  $\varnothing_{B,CT}^e$ , is compared with the idealised case,  $\varnothing_{B,ideal}^e$ , in Fig. 13. With the idealised shape factor for the circular cross-section being 1.0, the octagonal, square, and triangular cross-sections are 1.002, 1.047, and 1.209, respectively. Comparing  $\varnothing_{B,CT}^e$  to  $\varnothing_{B,ideal}^e$  shows the effect of manufacturing defects and control factors. The orientational dependence observed in  $I$  is again observed in  $\varnothing_B^e$ . The shape factor removes size dependence, so comparisons can be made purely on the achieved shape and not be confounded with whether more or less material is contributing to the change. Comparing  $\varnothing_B^e$  between aluminium (Fig. 13a–d)



**Fig. 11** Box plots of  $I_{CT}$  compared with  $I_{ideal}$  (green horizontal lines), where (a) to (d) are aluminium strut elements, with an effective diameter of 0.5 mm, 1.0 mm, 2.0 mm, and 3.0 mm, and (e) to (h) are titanium strut elements, with an effective diameter of 0.5 mm, 2.0 mm, and 3.0 mm (outliers hidden)



**Fig. 12** Box plots of  $R_{CT}$  compared with  $R_{ideal}$  (green horizontal lines), where (a) to (d) are aluminium strut elements, with an effective diameter of 0.5 mm, 1.0 mm, 2.0 mm, and 3.0 mm, and (e) to (h) are titanium strut elements, with an effective diameter of 0.5 mm, 1.0 mm, 2.0 mm, and 3.0 mm (outliers hidden)



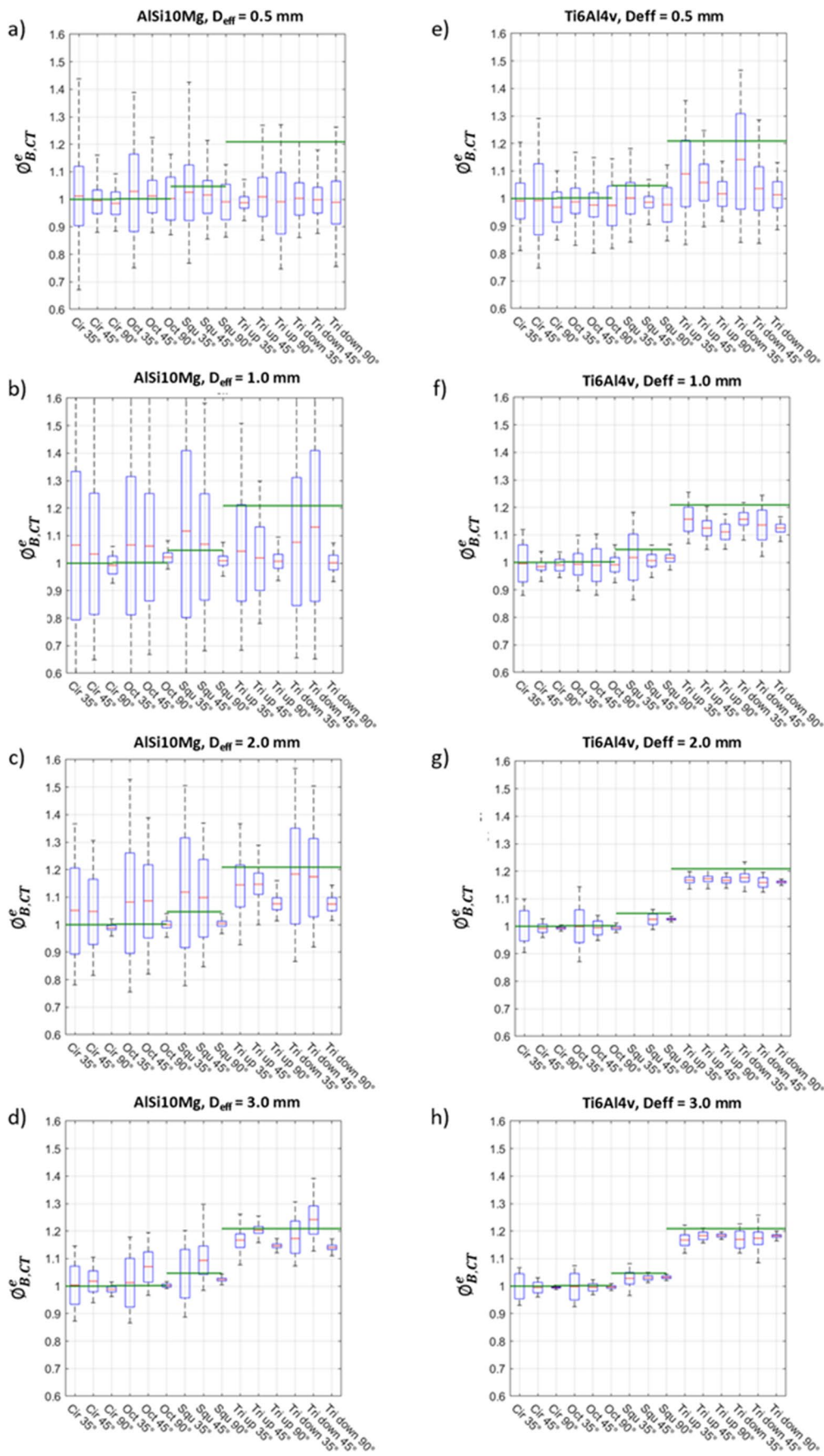


**Fig. 13** Box plots of CT stiffness shape factor,  $\varnothing_{B,CT}^e$ , compared with ideal stiffness shape factor,  $\varnothing_{B,ideal}^e$  (green horizontal lines), where (a) to (d) are aluminium strut elements, with an effective diameter of 0.5 mm, 1.0 mm, 2.0 mm, and 3.0 mm, and (e) to (h) are titanium strut elements, with an effective diameter of 0.5 mm, 1.0 mm, 2.0 mm, and 3.0 mm (outliers hidden)

and titanium (Fig. 13e–h), generally, there is less variability within individual titanium strut elements than within individual aluminium strut elements, as can be seen by the size of the IQR for individual box plots. This is most notable in the 35° and 45° cases. The exception appears to be in strut elements with smaller  $D_{eff}$  of 0.5 mm, where the aluminium and titanium both show relatively large variation in  $\varnothing_B^e$ . Also, at lower effective diameters, the elastic shape factors of the as-manufactured triangular cross-sections are producing results more in line with a circular cross-section. While at higher effective diameters, the elastic shape factor of the as-manufactured strut elements better matches the idealised trend for each shape. The transition for this behaviour occurs at  $D_{eff}$  of 1.0 mm for the titanium, and between an  $D_{eff}$  of 2.0 to 3.0 mm for the aluminium. Another observation is that the median  $\varnothing_B^e$  for the titanium strut elements lies at or below the ideal value; however, in the aluminium, particularly at an  $D_{eff}$  of 1.0 mm and 2.0 mm, the median  $\varnothing_B^e$  for the inclined circular, octagonal and square cross-sections lie above their ideal values. This appears to be an indication of defects introduced during MAM processes, suggesting that as-manufactured defects could increase local stiffness and failure response if they align favourably with loading conditions as illustrated in Fig. 8f; i.e., unintended additional material is deposited in such a way as to increase  $y_{max}$ , aligning with the optimal orientation.

#### 4.6 Failure shape factor (ideal versus CT)

The failure shape factor,  $\varnothing_B^f$ , can be used to evaluate the manufacturability of a strut element cross-section. With the idealised failure shape factor,  $\varnothing_{B,ideal}^f$ , for the circular cross-section being 1.0, the octagonal, square, and triangular cross-sections experience an orientation dependence and range from 0.95 to 1.029, 0.83 to 1.18, and 0.77 to 1.55, respectively. The failure shape factors for the as-manufactured strut elements,  $\varnothing_{B,CT}^f$ , are compared to the ideal ranges in Fig. 14. When comparing the aluminium (Fig. 14a–d) and titanium (Fig. 14e–h) cases, the titanium strut elements show greater consistency for a given shape across the three inclination angles, and the square and triangular shapes tend to remain bound by the ideal range, with the distributions better matching the ideal range with increasing effective diameter. This trend is not observed in the aluminium strut elements which show greater variation and is particularly apparent for circular and octagonal shapes. The large variation in the

failure shape factor highlights an opportunity for improved strength based on geometric orientation. An important observation from these graphs is that the median result typically sits below unity, meaning that most orientations result in reduced strength rather than improved strength. This indicates that care should be taken with cross-section orientation relative to the load direction.

#### 4.7 Main effect plots of section properties

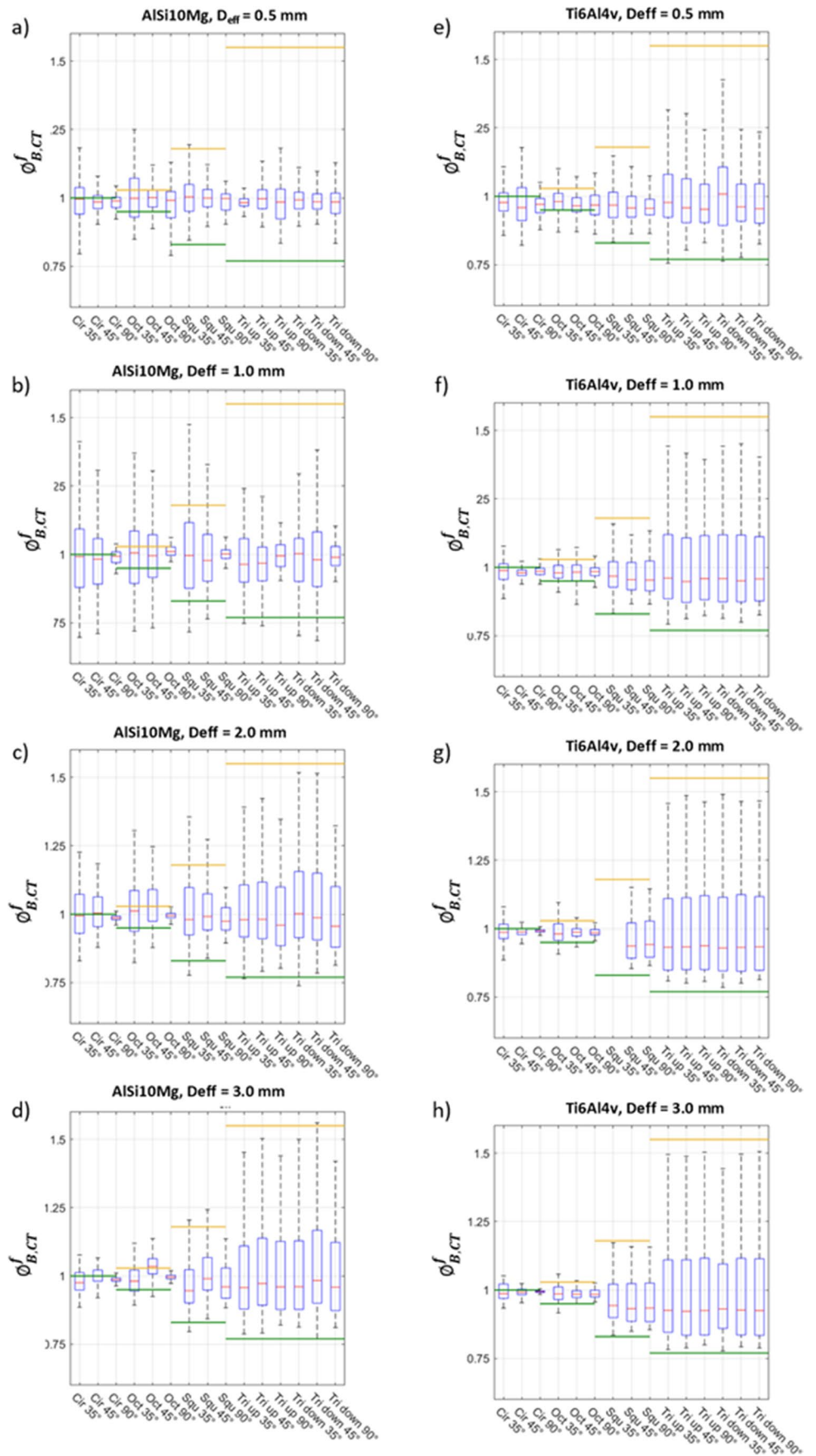
Main effect plots illustrate the influence of independent variables, or factors, on the dependent variables, as shown in Fig. 15, 16, 17, 18, and Fig. 19. The effect of the independent variable can be seen by the variation of the line, with a large deviation from the horizontal considered a significant effect. In this experiment, the independent variables affect each of the dependent variables, the manufactured section properties, to differing degrees. The effective diameter,  $D_{eff}$ , is the dominant factor for the cross-sectional area,  $A_{CT}$ , the second moment of area,  $I_{CT}$ , and the radius of gyration,  $R_{g,CT}$ . By contrast, the main effects of build angle, shape, and material on those section properties are relatively small. The main effects of the shape on the second moment of area shows  $I_{CT}$  improving as the polygon order decreases from circle to octagon, square, and finally triangle. However, the magnitude in variation is similar to that caused by the inclination angle,  $\alpha_{in}$ , and material. There is an expectation that the stiffness shape factor,  $\varnothing_B^e$ , and the failure shape factor,  $\varnothing_B^f$ , are independent of scale (i.e., the effective diameter,  $D_{eff}$ ), but dependent on the cross-sectional shape. The main effects plots for both the elastic,  $\varnothing_B^e$ , and failure shape factors,  $\varnothing_B^f$ , for manufactured struts, show that the shape variable is the most dominant, with the triangles giving the lowest values. However, the effective diameter,  $D_{eff}$ , also produces a significant effect. The material shows a small effect on all the section properties, with the titanium having slightly higher values than the aluminium.

### 5 Discussion

Structural mechanics theory suggests that of the regular polygons, square and triangular cross-sections provide the greatest structural efficiency over the circular cross-section, with elastic shape factors of 1.05 and 1.21, respectively, when aligned to the load direction. This suggests an opportunity for improved stiffness simply through the choice of more efficient cross-section shapes and aligning them to the load direction. For polygons with the equivalent cross-sectional area,  $I$  is the key parameter when considering stiffness and buckling resistance. For irregular cross-sections, both  $I$  and  $\varnothing_B^f$  have orientation dependencies. This orientation dependence is well known



**Fig. 14** Box plots of CT strength shape factor,  $\phi_{B,CT}^f$  of aluminium and titanium strut elements compared with a range of ideal strength shape factor,  $\phi_{B,ideal}^f$  values represented as green (lower value) and orange (upper value) horizontal lines, where (a) to (d) are aluminium strut elements, with an effective diameter of 0.5 mm, 1.0 mm, 2.0 mm, and 3.0 mm, and (e) to (h) are titanium strut elements, with an effective diameter of 0.5 mm, 1.0 mm, 2.0 mm, and 3.0 mm (outliers hidden)





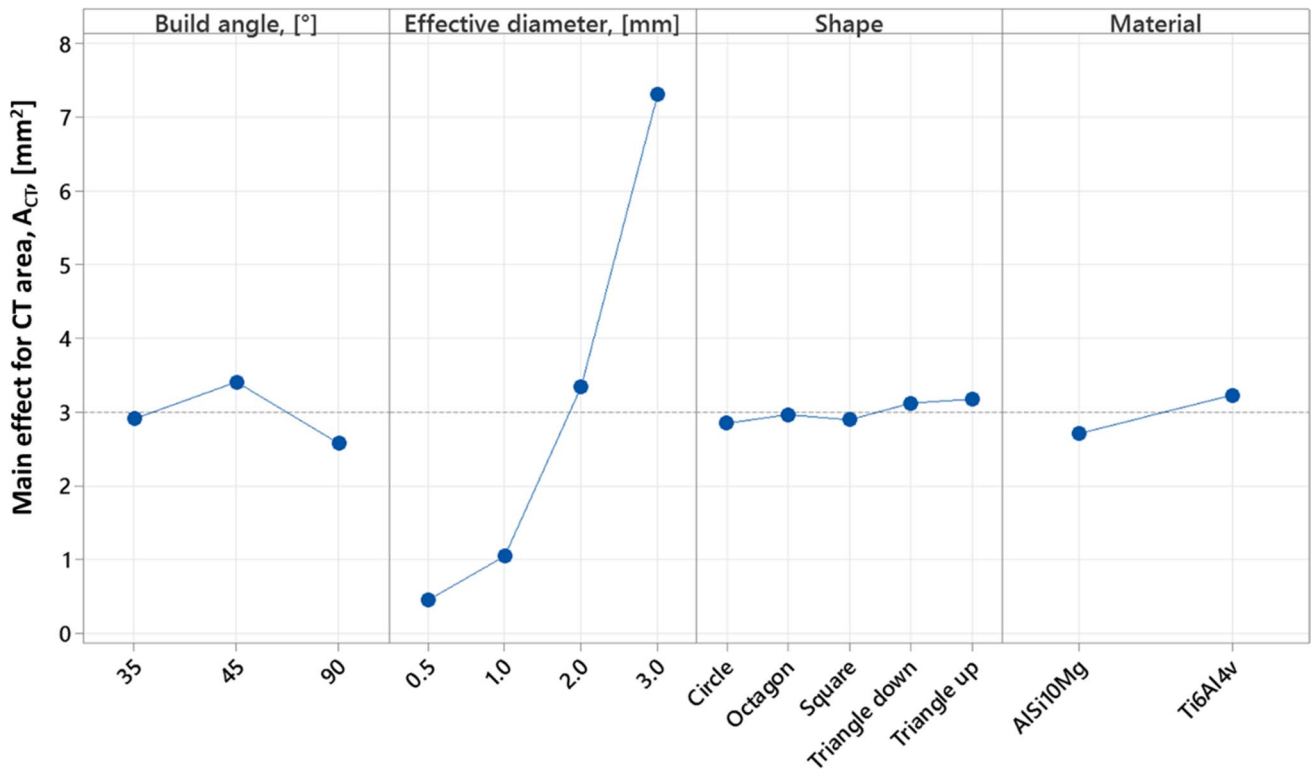


Fig. 15 Main effect plot for the CT area,  $A_{CT}$ , among independent variables

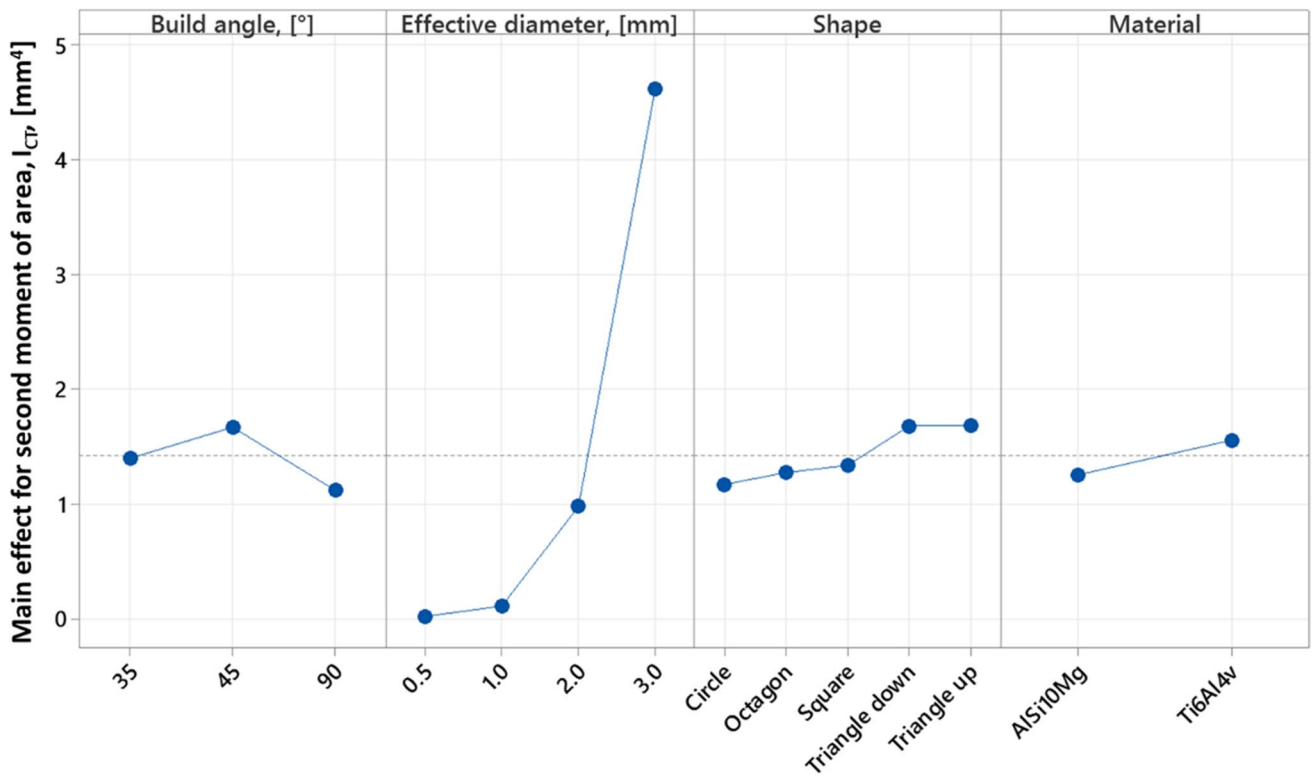


Fig. 16 Main effect plot for the second moment of area,  $I_{CT}$ , among independent variables

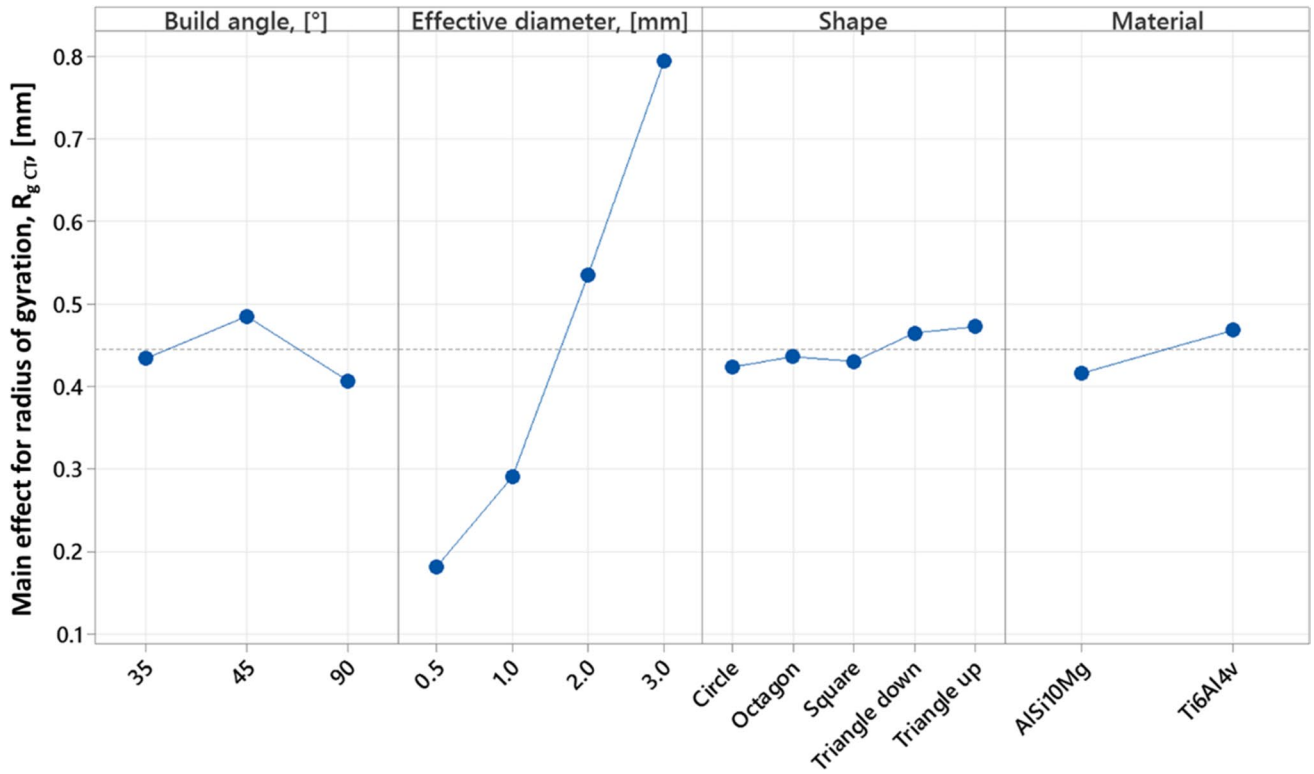


Fig. 17 Main effect plot for the radius of gyration,  $R_{g,CT}$ , among independent variables

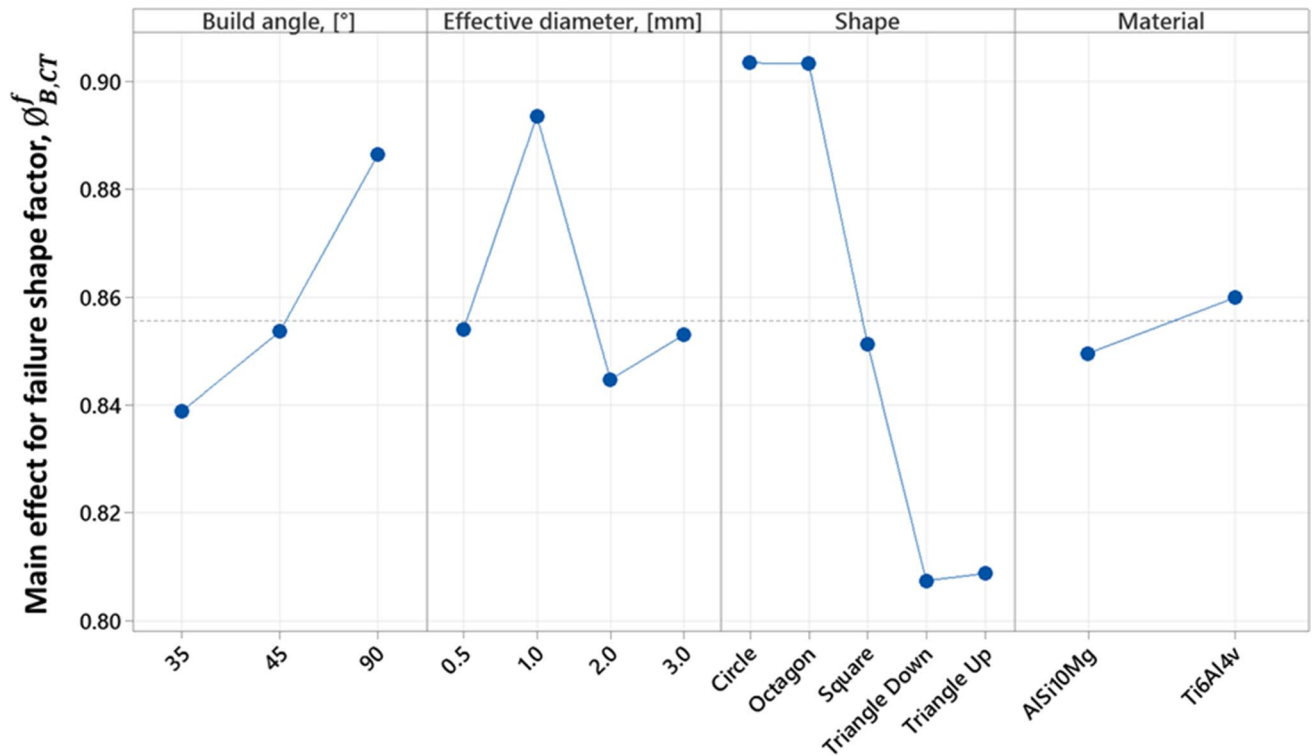


Fig. 18 Main effect plot for the elastic shape factor,  $\varphi_{B,CT}^e$ , among independent variables

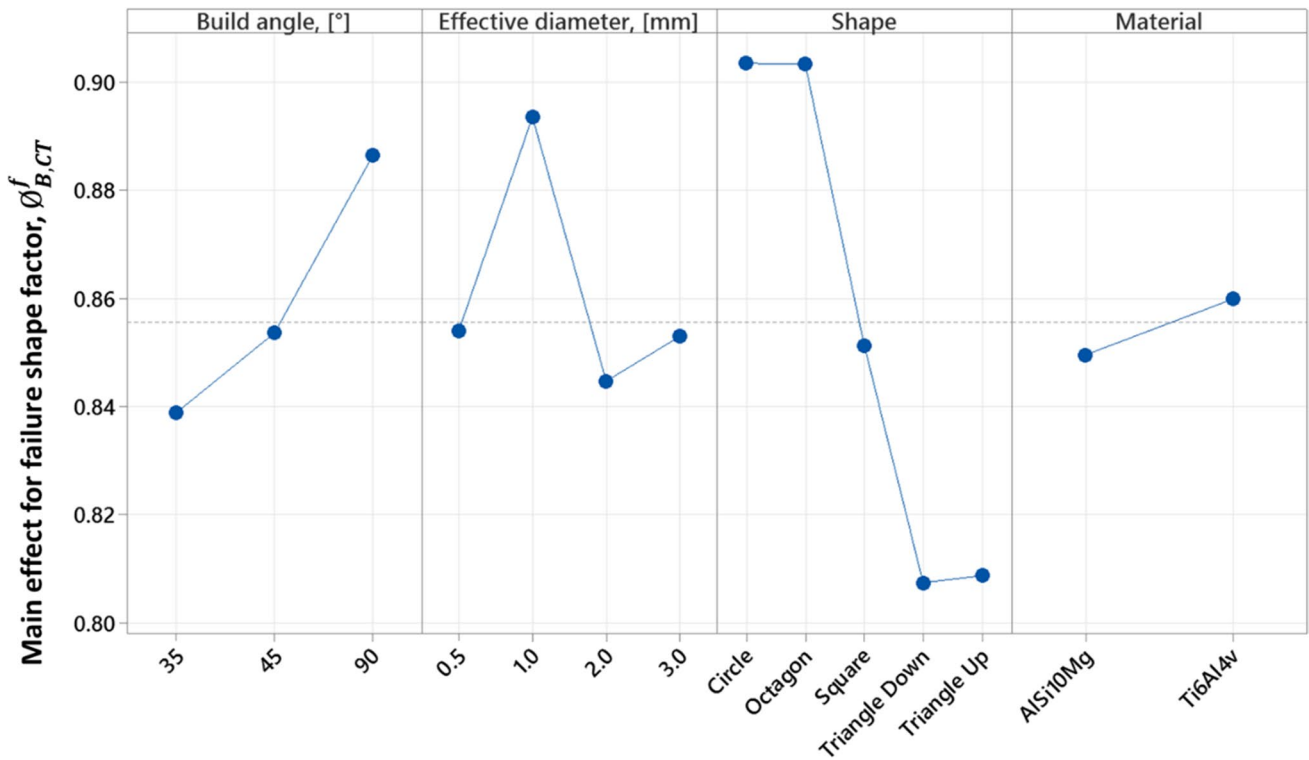


Fig. 19 Main effect plot for the minimum failure shape factor,  $\phi_{B,CT}^f$ , among independent variables

and exploited in the fields of civil and structural engineering through the use of shaped sections such as *I*-beams, although to date has yet to be applied to lattice structures. Given the failure shape factor’s dependence on orientation, it has been shown that strut elements are particularly sensitive to shape defects introduced during the AM process.

Titanium strut elements possessed more consistent geometric characteristics along their length of build for all sizes, although they exhibited an unexpected increase in cross-sectional area with decreasing polygon order. For square and triangular cross-sections,  $\phi_{B,CT}^e$  and  $\phi_{B,CT}^f$  approached the predicted values of  $\phi_{B,ideal}^e$  and  $\phi_{B,ideal}^f$  with increasing  $D_{eff}$ .

Aluminium strut elements were subject to significant variations in geometric characteristics along their length of build, with the shape being indistinguishable for results with an  $D_{eff}$  under 2 mm. A strong dependency on inclination angle,  $\alpha_{in}$ , was observed, with increasing cross-sectional area and variation in said area, a trend carried into all other characteristics. For the square and triangular cross-sections,  $\phi_{B,CT}^e$  and  $\phi_{B,CT}^f$  approached the predicted values of  $\phi_{B,ideal}^e$  and  $\phi_{B,ideal}^f$  with increasing  $D_{eff}$ , although results were lower than ideal when the  $D_{eff}$  was below 2 mm. A manufacturability limit of 2 mm is observed for all cross-sections in aluminium, with results below this being indistinguishable from the circular case.

To determine alternative cross-section shape suitability, the desired performance and the number of manufacturing defects that can be tolerated must be considered. For example, while a traditional *I*-beam section would provide exceptional stiffness, due to the thin sections of the web and flanges, they would be particularly susceptible to defects at small scales and it is only appropriate for two diametrically opposed loading conditions; in complex loading conditions, this section is less than optimal. The second moment of area of regular polygons is independent of the loading direction (unlike irregular polygons). Thus, resistance to elastic bending could be improved by switching to the triangular or square cross-section, regardless of load direction.

There are future opportunities to extend the methodology and analysis to other loading cases, cross-sections, and materials. Both  $\phi_B^e$ , characterising elastic bending and buckling resistance, and  $\phi_B^f$ , characterising bending failure, have been considered as these are often the dominant behaviours in lattice structures under compression. Other shape factors, such as torsion, must be considered for more complex loading cases. This could lead to an investigation of alternative cross-sections that provide structural efficiencies, such as channels and hollow sections [32]. Furthermore, this methodology can be applied to investigate the manufacturability and as-manufactured structural efficiency of other AM systems [24, 25] and materials.

## 6 Summary

Laser-based powder bed fusion processes observe a high frequency of geometrical variation between the idealised models and the as-manufactured specimens. This research has developed a design tool to algorithmically quantify the structural impact of as-manufactured geometrical defects.

The as-manufactured strut elements were imaged using  $\mu$ CT and then reconstructed into a stack of as-manufactured strut element cross-section images. The geometric parameters including,  $A_{CT}$ ,  $I_{CT}$ ,  $\varnothing_{B,CT}^e$ , and  $\varnothing_{B,CT}^f$  have been quantified using the proposed method and verified against idealised cases.

The methodology was applied to two sets of additively manufactured strut elements, one in aluminium alloy AlSi10Mg and another in titanium alloy Ti6Al4V, with varying effective diameters, polygon orders, and inclination angles. The following key observations were made.

- $I_{ideal}$  for the square and triangular cross-sections have a 5% and 21% improvement, respectively, compared to the idealised circular cross-section. This indicates an increased elastic buckling and bending resistance of fabricated strut elements.
- $I_{ideal}$  of circular and octagonal cross-sections differ by only 0.2%, displaying that polygon orders greater than eight do not significantly affect  $I$ . This is most beneficial as representing struts with larger order polygons typically require larger file sizes. These file size requirements may then be reduced without losing as-manufactured shape accuracy. Fewer faces also benefit FEA, with lower computational costs.
- It was found that the variation between  $I_{CT}$  and  $I_{ideal}$  in aluminium is generally greater than that in titanium, indicating titanium produces less manufacturing defects. These variations are increased with lower inclination angles,  $\alpha_{in}$ .
- The effective diameter has a major impact on the manufacturability of the strut elements, particularly on aluminium at  $D_{eff} \leq 2.0$  mm. At these sizes, the variation in the dependent variables is significantly larger than the expected ranges and the effect of shape is not discernible over the inclination angle. A transition is seen at  $D_{eff} = 3.0$  mm, where the aluminium struts show dependence on shape and inclination angle. For titanium, this transition is more apparent between 0.5 and 1.0 mm
- $\varnothing_B^e$  and  $\varnothing_B^f$  are useful to determine the manufacturability of different regular polygon cross-sections. As the effective diameter increased,  $\varnothing_{B,CT}^e$  and  $\varnothing_{B,CT}^f$  distributions were more closely aligned with the range of their idealised values,  $\varnothing_{B,ideal}^e$  and  $\varnothing_{B,ideal}^f$ , indicating greater accuracy in achieving idealised geometry. Titanium strut

elements show this improvement in both  $\varnothing_{B,CT}^e$  and  $\varnothing_{B,CT}^f$ , for each incremental increase in  $D_{eff}$ . Aluminium strut elements show poor replication of both shape factors at all but the largest effective diameter.

- The main effects analysis showed that the effective diameter is the dominant factor for strut cross-sectional area, second moment of area, and radius of gyration. The shape was the dominant factor for the elastic shape factor and failure shape factor; however, effective diameter and build angle also had a strong influence.

## 7 Future work

Future work will be dedicated to exploring the production of parts using multi jet fusion (MJF), which can fabricate parts significantly faster than LB-PBF, using the developed methodology to determine the manufacturability and mechanical responses of parts fabricated using the MJF process. The comparison of this work and producing parts using MJF opens up the possibility of better understanding the advantage and disadvantages of each process relative to the required application. Porosity also will be considered as one of the section properties that affect the manufacturable and mechanical performance.

**Acknowledgements** The authors acknowledge the use of facilities within RMIT Advanced Manufacturing Precinct and the RMIT Microscopy and Microanalysis Facility. (<https://www.rmit.edu.au/about/our-locations-and-acilities/facilities/researchfacilities/advanced-manufacturing-precinct>).

**Funding** Open Access funding enabled and organized by CAUL and its Member Institutions

**Data availability** The data is available and only can be provided by request of the journal.

**Code availability** The code is available and only can be provided by request of the journal.

## Declarations

**Ethics approval** Not applicable.

**Consent to participate** Not applicable.

**Consent for publication** Not applicable.

**Competing interests** The authors declare no competing interests.

**Open Access** This article is licensed under a Creative Commons Attribution 4.0 International License, which permits use, sharing, adaptation, distribution and reproduction in any medium or format, as long as you give appropriate credit to the original author(s) and the source, provide a link to the Creative Commons licence, and indicate if changes were made. The images or other third party material in this article are included in the article's Creative Commons licence, unless indicated

otherwise in a credit line to the material. If material is not included in the article's Creative Commons licence and your intended use is not permitted by statutory regulation or exceeds the permitted use, you will need to obtain permission directly from the copyright holder. To view a copy of this licence, visit <http://creativecommons.org/licenses/by/4.0/>.

## References

- Gibson I et al (2021) Additive manufacturing technologies. Springer International Publishing
- Leary M, Mazur M, Williams H, Yang E, Alghamdi A, Lozanovski B, Shidid D, Farahbod-Sternahl L, Witt G, Kelbassa I, Choong P, Qian M, Brandt M (2018) Inconel 625 lattice structures manufactured by selective laser melting (SLM): mechanical properties, deformation and failure modes. *Mater Des* 157:179–199
- Mun J, Ju J, and Thurman J (2014) Indirect additive manufacturing based casting (I AM casting) of a lattice structure. in ASME International Mechanical Engineering Congress and Exposition, Proceedings (IMECE).
- Frazier WE (2014) Metal additive manufacturing: a review. *J Mater Eng Perform* 23(6):1917–1928
- Alghamdi A et al (2019) Effect of polygon order on additively manufactured lattice structures: a method for defining the threshold resolution for lattice geometry. *Int J Adv Manuf Technol* 105:2501–2511
- Leary M et al (2018) Inconel 625 lattice structures manufactured by selective laser melting (SLM): mechanical properties, deformation and failure modes. *Mater Des* 157:179–199
- Lozanovski B et al (2019) Computational modelling of strut defects in SLM manufactured lattice structures. *Mater Des* 171:107671
- Zhai X, Jin L, Jiang J (2022) A survey of additive manufacturing reviews. *MSAM* 1(4):21
- Downing D et al (2020) Heat transfer in lattice structures during metal additive manufacturing: numerical exploration of temperature field evolution. *Rapid Prototyp J* 25(5):911–928
- Zhang B, Li Y, Bai Q (2017) Defect formation mechanisms in selective laser melting: a review. *Chin J Mech Eng* 30(3):515–527
- Echeta I et al. (2019) Review of defects in lattice structures manufactured by powder bed fusion. *Int J Adv Manuf Technol*, 1–20.
- Leary M et al. (2021) Surface roughness, in *Fundamentals of Laser Powder Bed Fusion of Metals*, I. Yadroitsev, et al., Editors.
- Li R et al (2012) Balling behavior of stainless steel and nickel powder during selective laser melting process. *Int J Adv Manuf Technol* 59(9):1025–1035
- Alghamdi A et al. (2020) Effect of additive manufactured lattice defects on mechanical properties: an automated method for the enhancement of lattice geometry. *Int J Adv Manuf Technol*, 1–15.
- Ali H, Ghadbeigi H, Mumtaz K (2018) Processing parameter effects on residual stress and mechanical properties of selective laser melted Ti6Al4V. *J Mater Eng Perform* 27(8):4059–4068
- Alomar Z, Concli F (2020) A review of the selective laser melting lattice structures and their numerical models. *Adv Eng Mater* 12(12):2000611
- Noronha J et al (2021) Manufacturability of Ti-Al-4V hollow-walled lattice struts by laser powder bed fusion. *JOM* 73(12):4199–4208
- Bächle M, Kohal RJ (2004) A systematic review of the influence of different titanium surfaces on proliferation, differentiation and protein synthesis of osteoblast-like MG63 cells. *Clin Oral Implants Res* 15(6):683–692
- Zhang XZ et al (2018) Toward manufacturing quality Ti-6Al-4V lattice struts by selective electron beam melting (SEBM) for lattice design. *Jom* 70(9):1870–1876
- Shidid D et al (2016) Just-in-time design and additive manufacture of patient-specific medical implants. *Phys Procedia* 83:4–14
- Fleck NA (2002) New approaches to structural mechanics, shells and biological structures kluwer. *New Approaches to Structural Mechanics, Shells and Biological Structures*. Springer Netherlands : Imprint: Springer.
- Deshpande VS, Fleck NA, Ashby MF (2001) Effective properties of the octet-truss lattice material. *J Mech Phys Solids* 49(8):1747–1769
- Maconachie T et al. (2021) The effect of topology on the quasi-static and dynamic behaviour of SLM AlSi10Mg lattice structures. *Int J Adv Manuf Technol*.
- Kang D et al (2019) Multi-lattice inner structures for high-strength and light-weight in metal selective laser melting process. *Mater Des* 175:107786
- Clifford M, Simmons K, Shipway P (2009) An introduction to mechanical engineering: Part 1. CRC Press
- Gentle R, Edwards P, Bolton W (2001) Mechanical engineering systems. Elsevier, pp 261–265
- Hally D (1987) Calculation of the moments of polygons. Defence Research Establishment Suffield Ralston (Alberta)
- Ochshorn J (2009) Structural elements for architects and builders. Elsevier
- Alghamdi A et al (2021) Buckling phenomena in AM lattice strut elements: a design tool applied to Ti-6Al-4V LB-PBF. *Mater Des* 208:109
- Ashby MF, Cebon D (1993) Materials selection in mechanical design. *Le J de Phys IV* 3(C7):C7–C1
- Almalki A et al (2022) A digital-twin methodology for the non-destructive certification of lattice structures. *JOM* 74(4):1784–1797
- Jywe W-Y, Liu C-H, Chen CO-K (1999) The min-max problem for evaluating the form error of a circle. *Measurement* 26(4):273–282

**Publisher's note** Springer Nature remains neutral with regard to jurisdictional claims in published maps and institutional affiliations.